Supplementary Information for

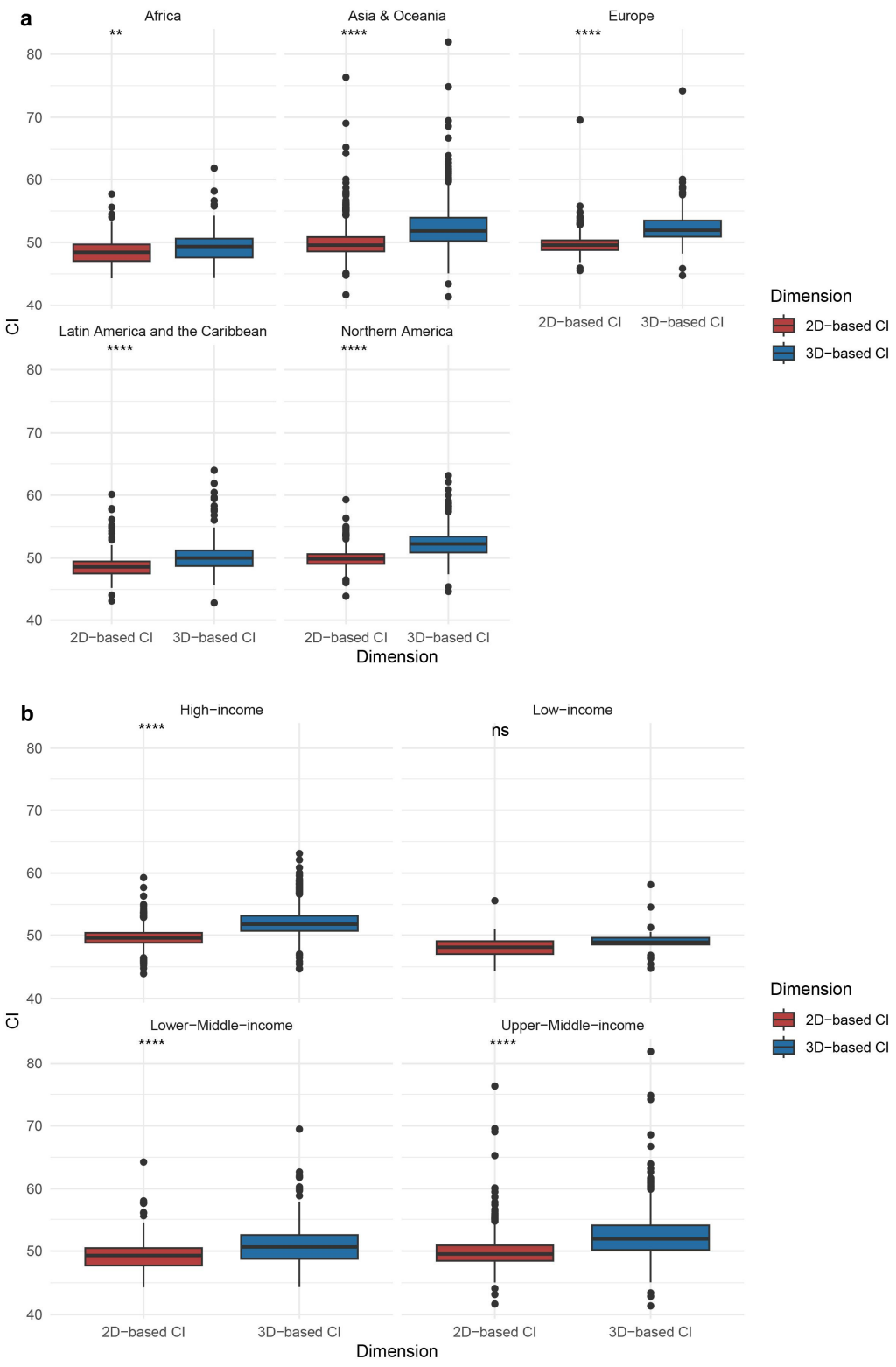
Global Increases in Built-Up Volume Indicate More Divergent and Less Dispersed Urban Expansion Patterns

Yingcheng Li[1, *], Xiaohan Zhong[1], Ben Derudder[2, 3, 4], Mingxing Hu[1], Xingjian Liu[5, *]

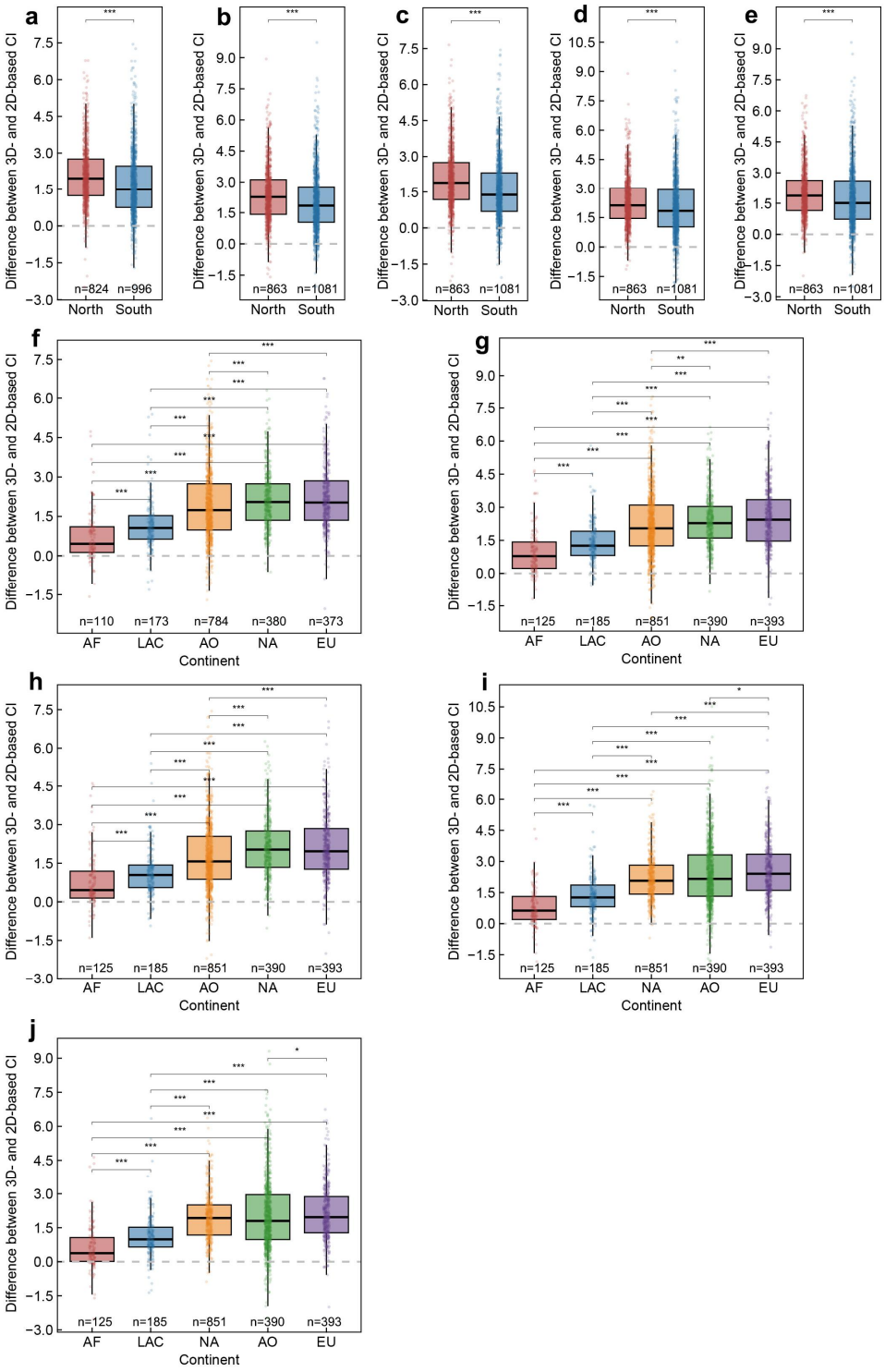
[1] School of Architecture, Southeast University, Nanjing, China
[2] Public Governance Institute, KU Leuven, Leuven, Belgium
[3] Department of Urban Studies and Sustainable Development, Nicolaus Copernicus University, Torun, Poland
[4] Department of Geography, Ghent University, Ghent, Belgium
[5] Faculty of Architecture, Department of Urban Planning and Design, The University of Hong Kong, Hong Kong, China
[*]Co-corresponding authors: lychls@seu.edu.cn (Yingcheng Li)
xliu6@hku.hk (Xingjian Liu)

Contents

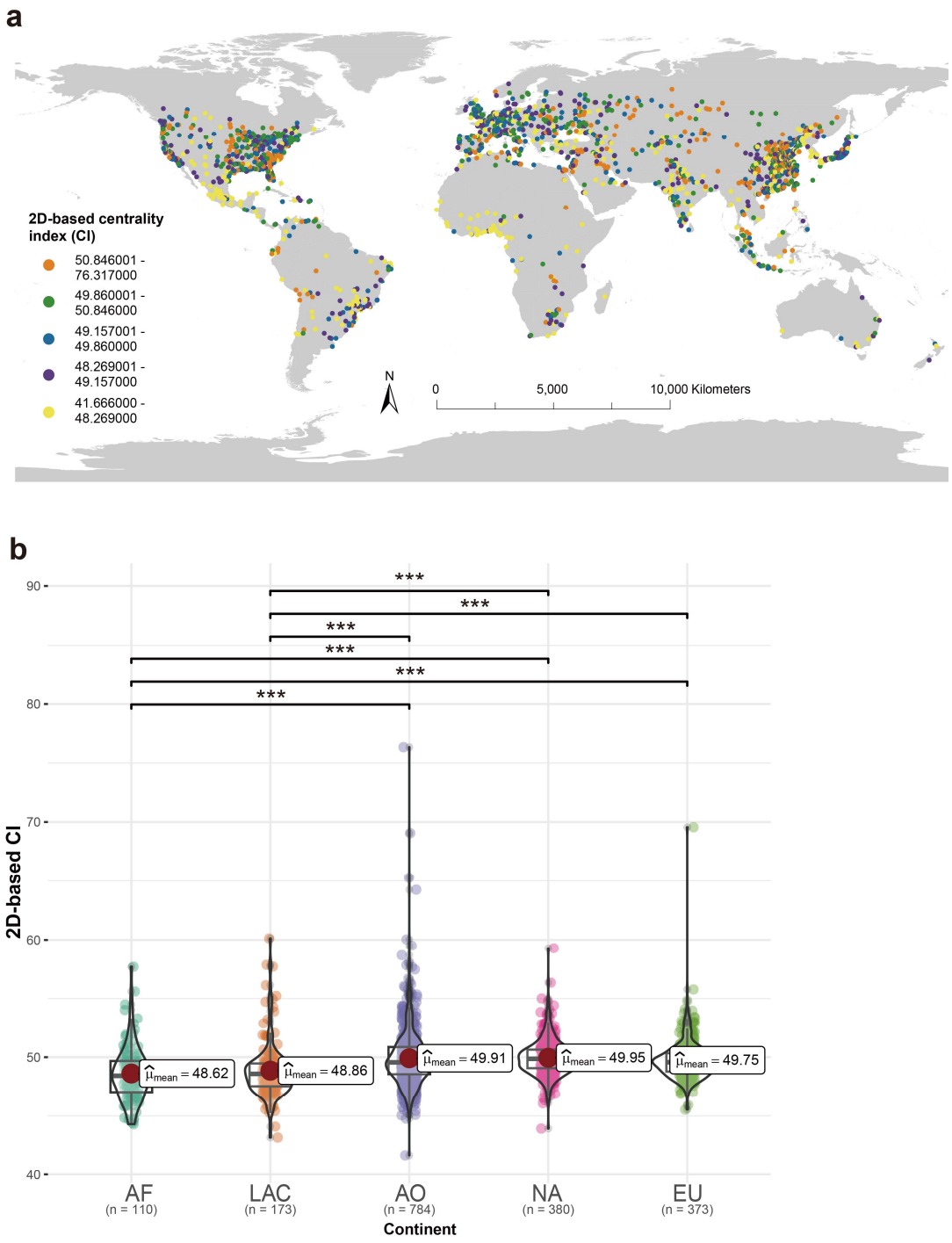
Supplementary Figure 1. 1
Supplementary Figure 2. 2
Supplementary Figure 3. 3
Supplementary Figure 4. 4
Supplementary Figure 5. 5
Supplementary Figure 6. 6
Supplementary Figure 7. 7
Supplementary Figure 8. 8
Supplementary Figure 9. 9
Supplementary Figure 10. 10
Supplementary Figure 11. 11
Supplementary Figure 12. 12
Supplementary Figure 13. 13
Supplementary Figure 14. 14
Supplementary Figure 15. 15
Supplementary Figure 16. 16
Supplementary Figure 17. 17
Supplementary Figure 18. 18
Supplementary Figure 19. 19
Supplementary Table 1. 20
Supplementary Table 2. 22
Supplementary Table 3. 23
Supplementary Table 4. 26
Supplementary Note 1. Independence Tests between 2D- and 3D-based CI 28
Supplementary Note 2. Independence Tests between 3D-based CI and II 29
Supplementary Note 3. Robustness Tests of Classification Methods 30
Supplementary Table 5. 31
Supplementary Table 6. 32
Supplementary Figure 20. 32
Supplementary Figure 21. 33
Supplementary Figure 22. 34
Supplementary Figure 23. 35
Supplementary Note 4. LightGBM Model Evaluation and Interpretation 36
Supplementary Table 7. 37
Supplementary Note 5. Impact Assessment of Exclusion of Urban Renewal 38
Supplementary Table 8. 39
Supplementary References 41



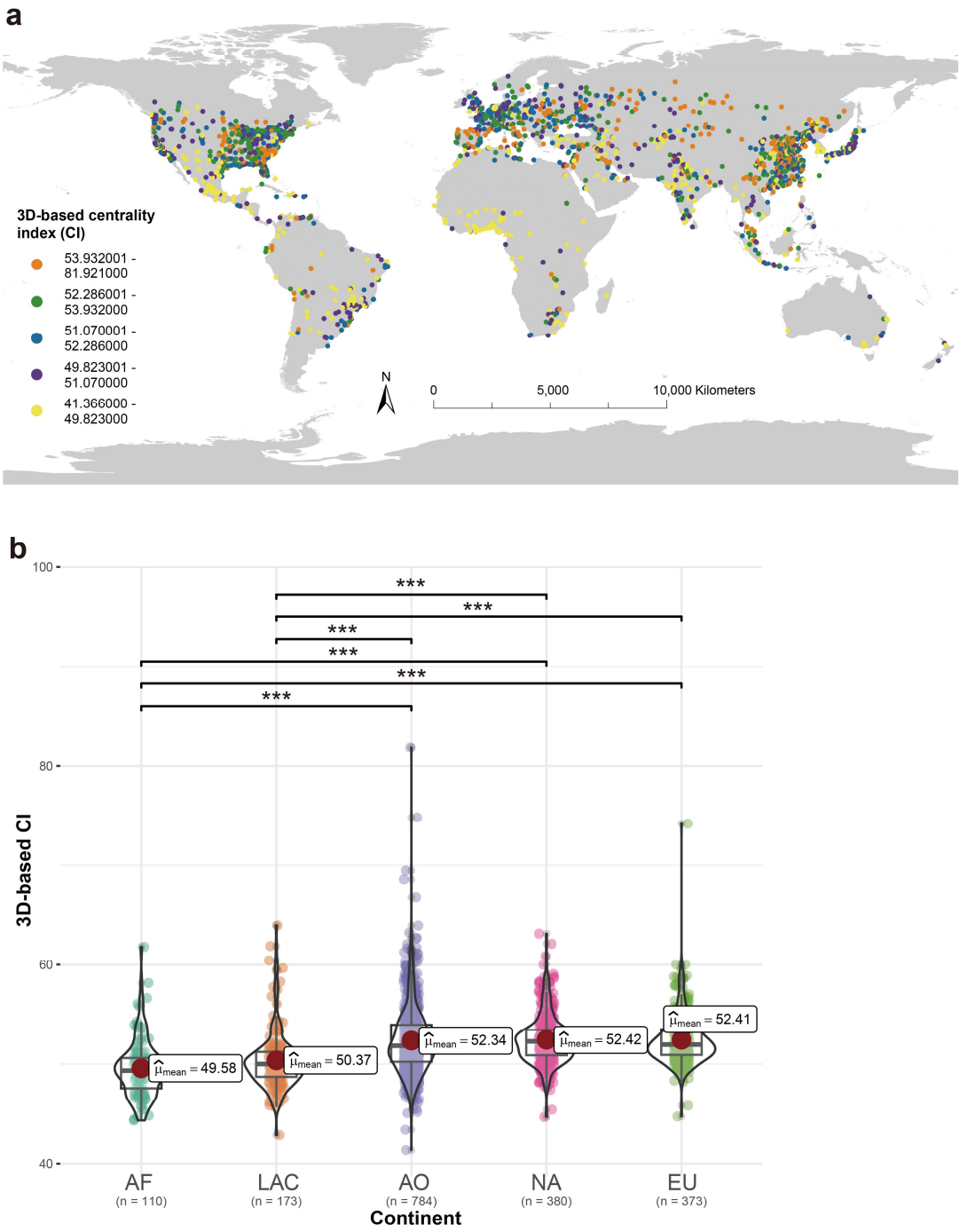
Supplementary Figure 1. Centrality Index (CI) comparison between 2D- and 3D-based measurements. **a** CI difference across different continents. **b** CI differences across World Bank's income level groups of countries The significance test is Mann-Whitney U test (two-tailed). **** p<0.0001, *** p<0.001, ** p<0.01, * p<0.05, ns not significant.



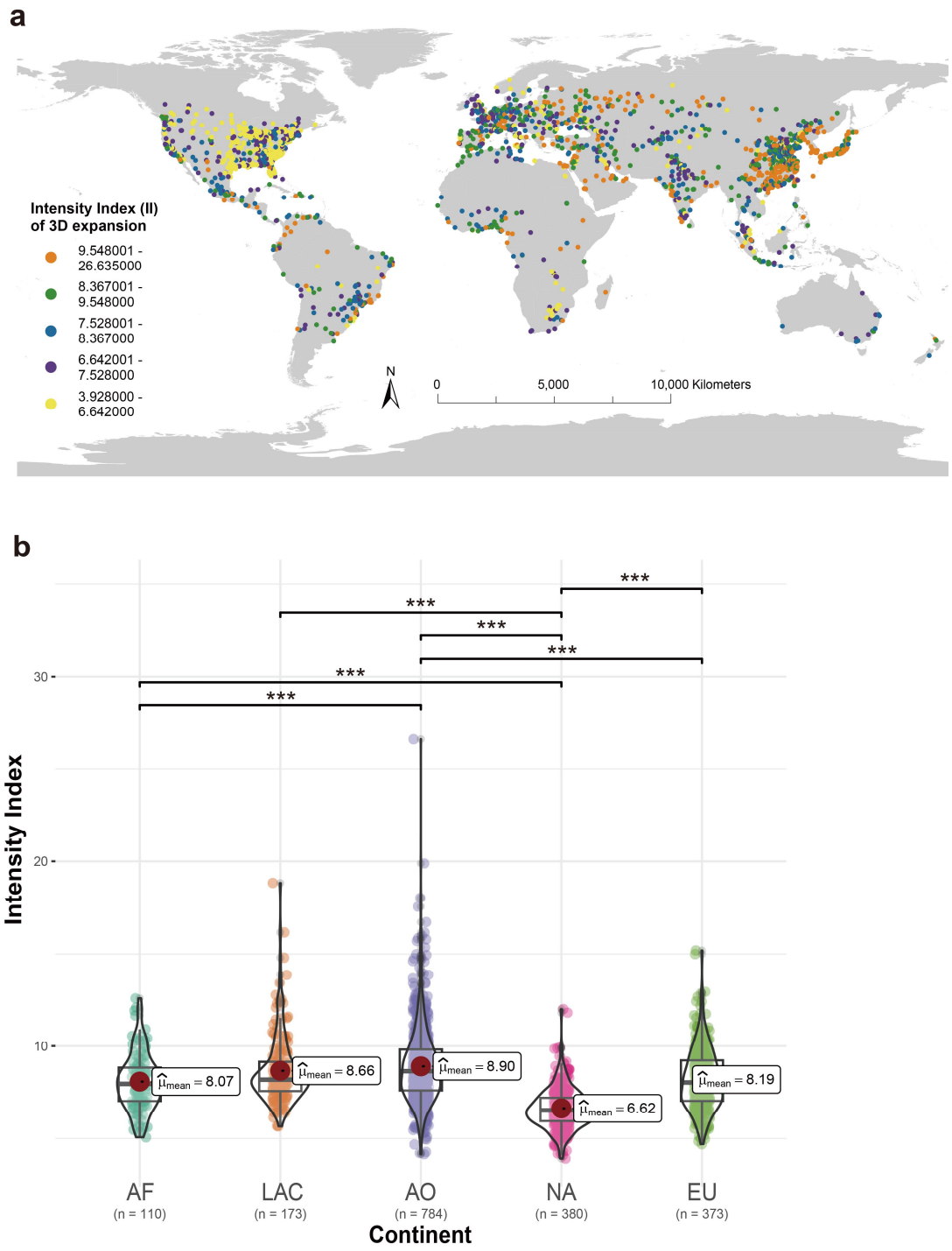
Supplementary Figure 2. Centrality Index score differences calculated using five alternative data combinations. **a** and **f**, the combination of selected increased built-up volume and integrated center. **b** and **g**, the combination of all increased built-up volume and population center. **c** and **h**, the combination of selected increased built-up volume and population center. **d** and **i**, the combination of all increased built-up volume and nighttime-light center. **e** and **j**, the combination of selected increased built-up volume and nighttime-light center. The significance test is Mann-Whitney U test (two-tailed). *** $p<0.001$, ** $p<0.01$, * $p<0.05$.



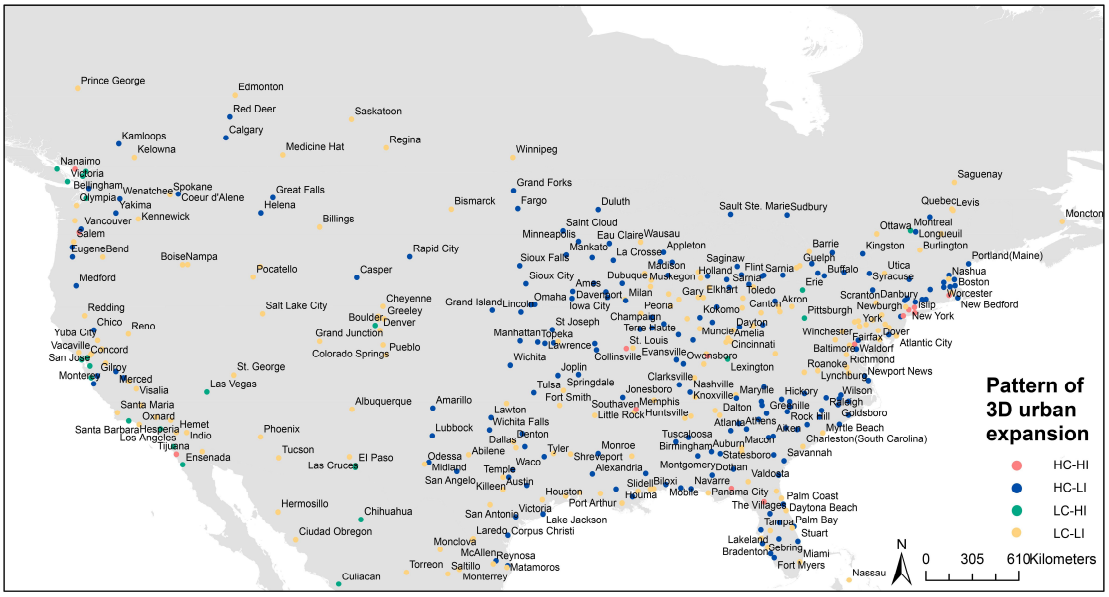
Supplementary Figure 3. Analyses of 2D-based Centrality Index (CI). a Geographical distribution of the 2D-based CI across 1820 sample cities. The five levels are divided by quantile. Maps were created using ArcGIS® software by Esri. Basemap polygon data source: Resource and Environmental Science Data Platform (https://www.resdc.cn/data.aspx?DATAID=205). **b** 2D-based CI score differences across continents or regions. Abbreviations: AF, Africa; LAC, Latin America and the Caribbean; AO, Asia and Oceania; NA, North America; EU, Europe. Statistical significance was tested using the Mann-Whitney U test (two-tailed). *** $p<0.001$, ** $p<0.01$, * $p<0.05$.



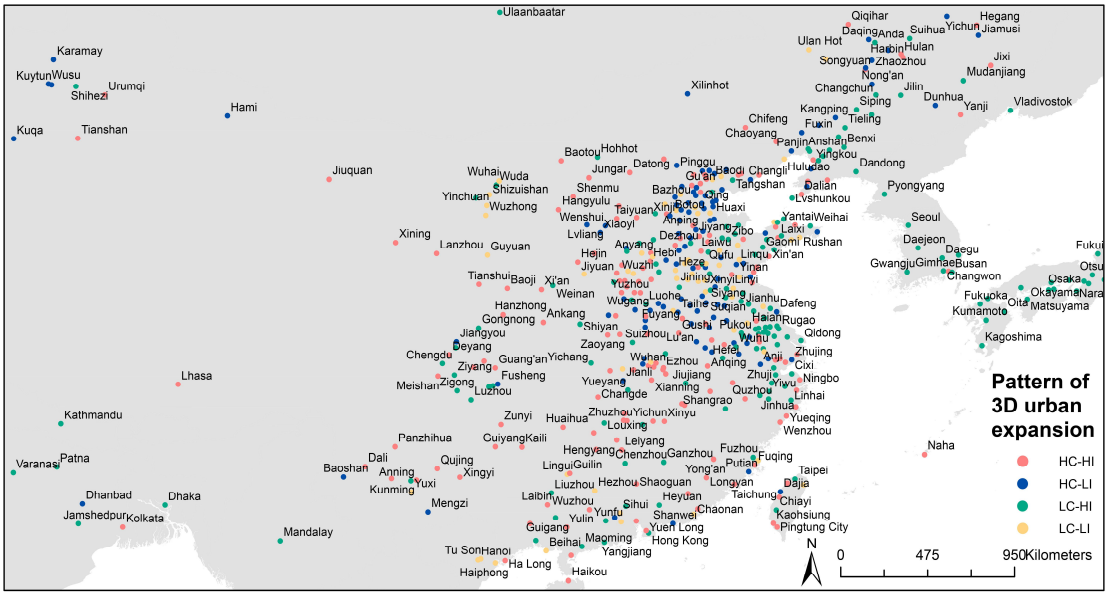
Supplementary Figure 4. Analyses of 3D-based Centrality Index (CI). a Geographical distribution of the 3D-based CI across 1820 sample cities. The five levels are divided by quantile. Maps were created using ArcGIS® software by Esri. Basemap polygon data source: Resource and Environmental Science Data Platform (https://www.resdc.cn/data.aspx?DATAID=205). **b** 3D-based CI score differences across continents or regions. Abbreviations: AF, Africa; LAC, Latin America and the Caribbean; AO, Asia and Oceania; NA, North America; EU, Europe. Statistical significance was tested using the Mann-Whitney U test (two-tailed). *** $p<0.001$, ** $p<0.01$, * $p<0.05$.



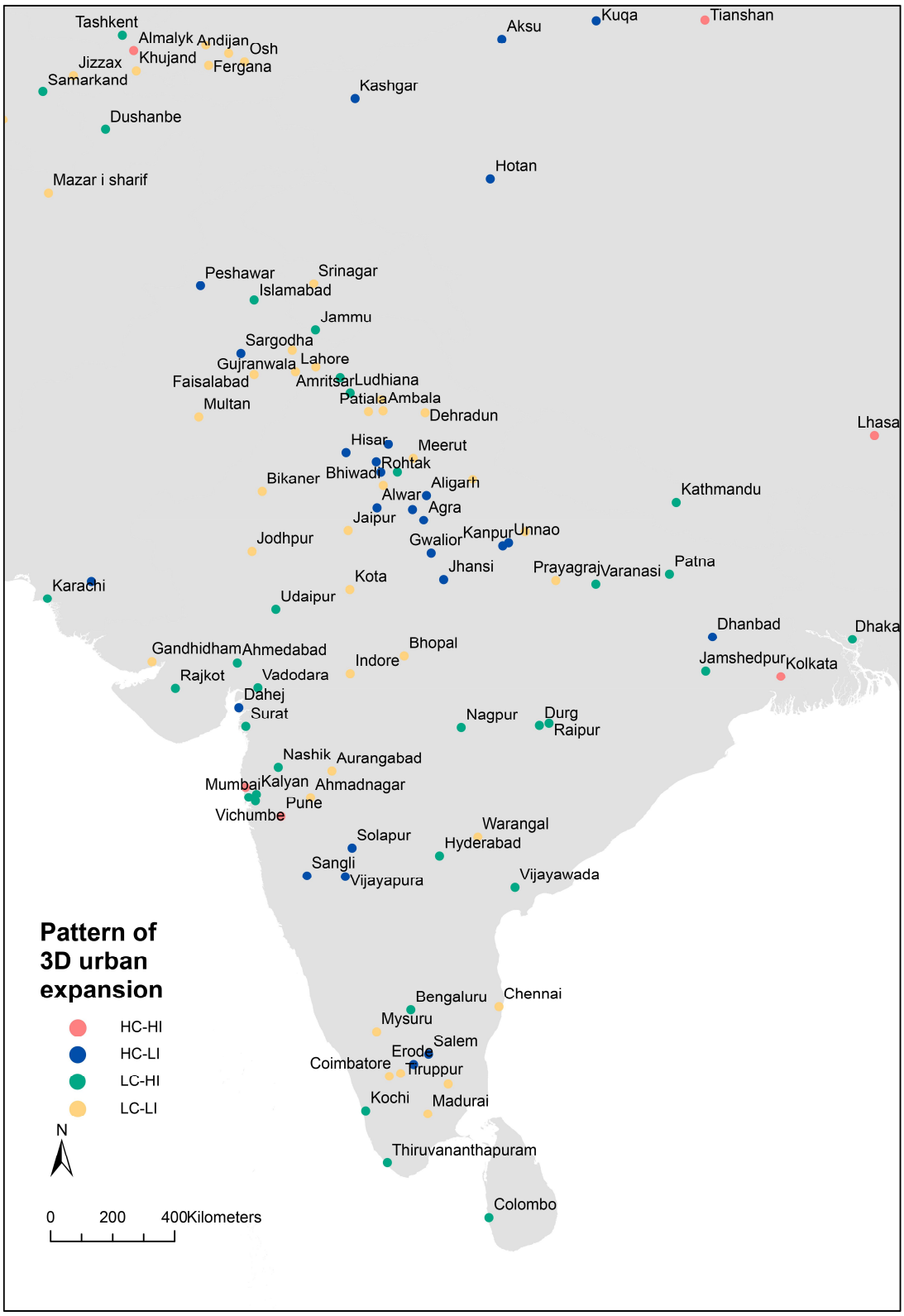
Supplementary Figure 5. Analyses of Intensity Index (II). a Geographical distribution of II across 1820 sample cities. Each dot represents a sample city. The five levels are divided by quantile. Maps were created using ArcGIS® software by Esri. Basemap polygon data source: Resource and Environmental Science Data Platform (https://www.resdc.cn/data.aspx?DATAID=205). **b** II score differences across continents or regions. Abbreviations: AF, Africa; LAC, Latin America and the Caribbean; AO, Asia and Oceania; NA, North America; EU, Europe. Statistical significance was tested using the Mann-Whitney U test (two-tailed). *** $p<0.001$, ** $p<0.01$, * $p<0.05$.



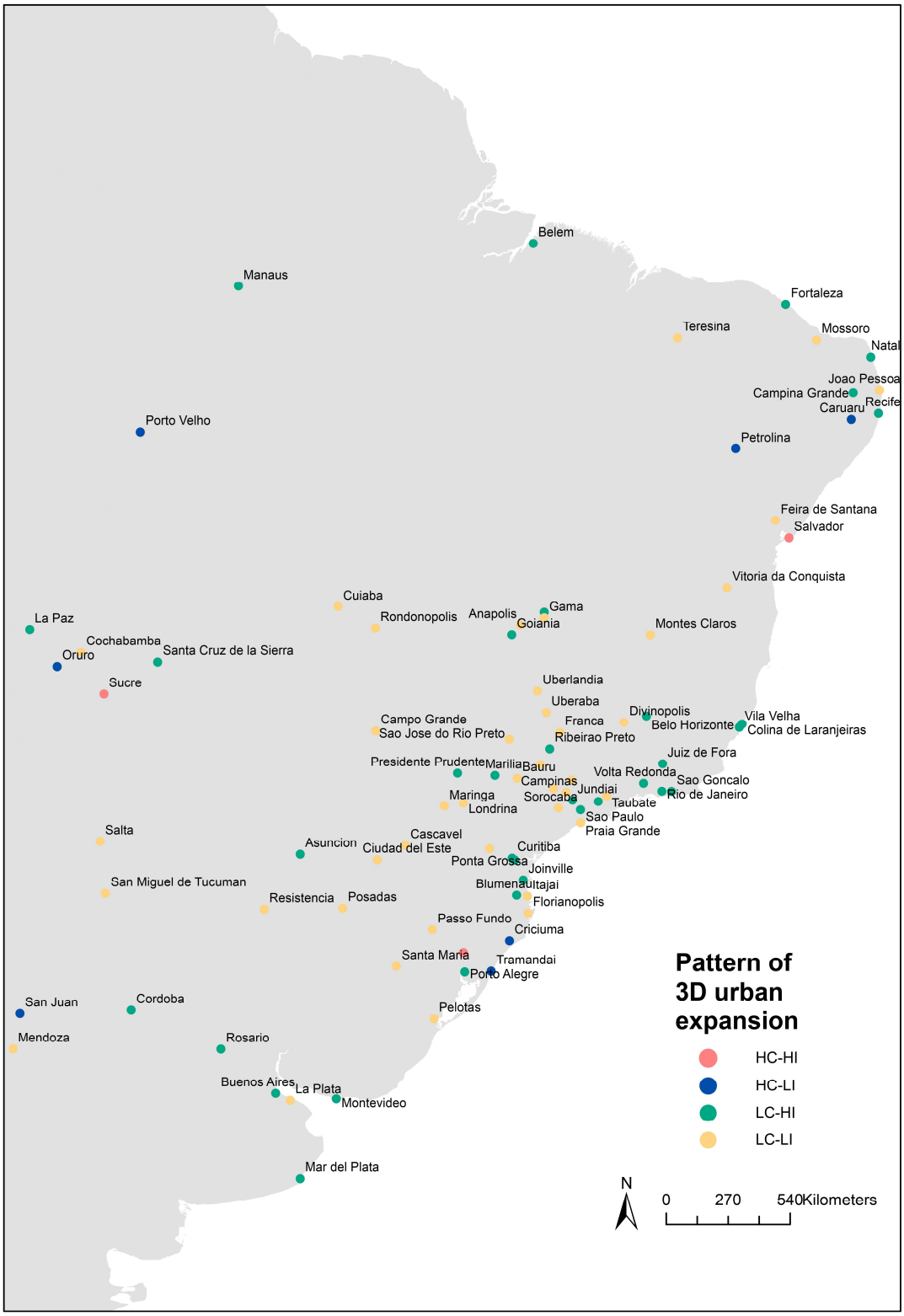
Supplementary Figure 6. Geographical distribution of 3D urban expansion patterns in the US and North America. Each dot represents a sample city. Maps were created using ArcGIS® software by Esri. Basemap polygon data source: Resource and Environmental Science Data Platform (https://www.resdc.cn/data.aspx?DATAID=205)



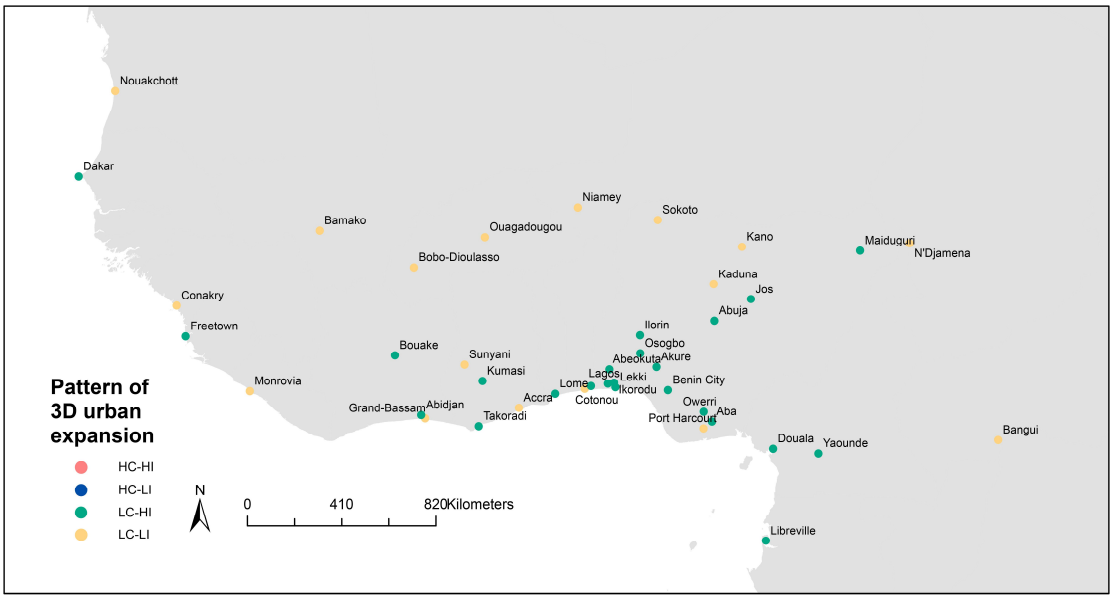
Supplementary Figure 7. Geographical distribution of 3D urban expansion patterns in China and East Asia. Each dot represents a sample city. Maps were created using ArcGIS® software by Esri. Basemap polygon data source: Resource and Environmental Science Data Platform (https://www.resdc.cn/data.aspx?DATAID=205)



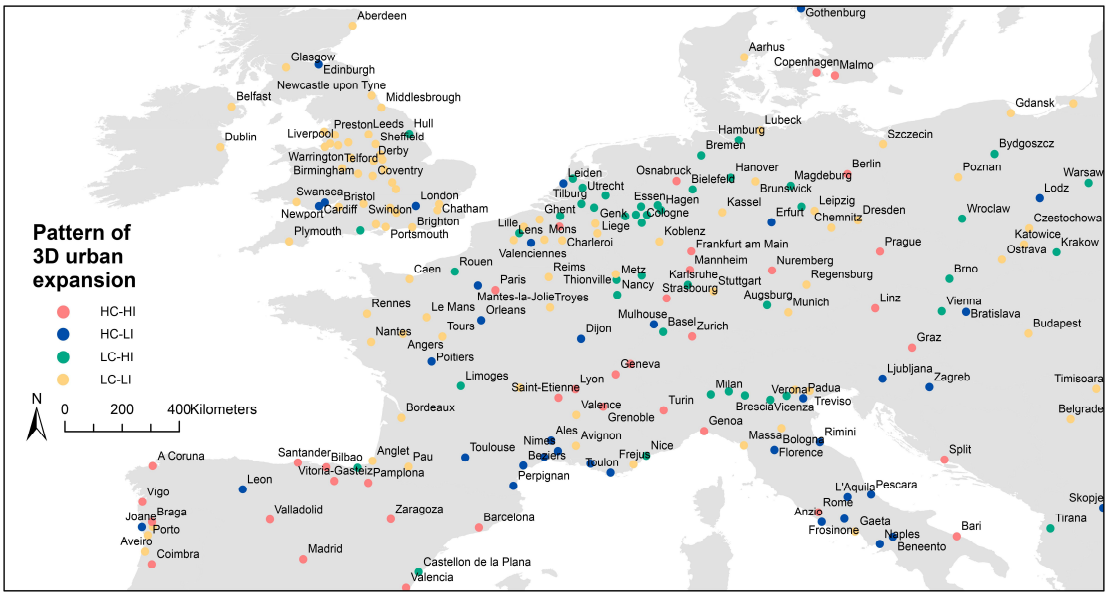
Supplementary Figure 8. Geographical distribution of 3D urban expansion patterns in India and South Asia. Each dot represents a sample city. Maps were created using ArcGIS® software by Esri. Basemap polygon data source: Resource and Environmental Science Data Platform (https://www.resdc.cn/data.aspx?DATAID=205)



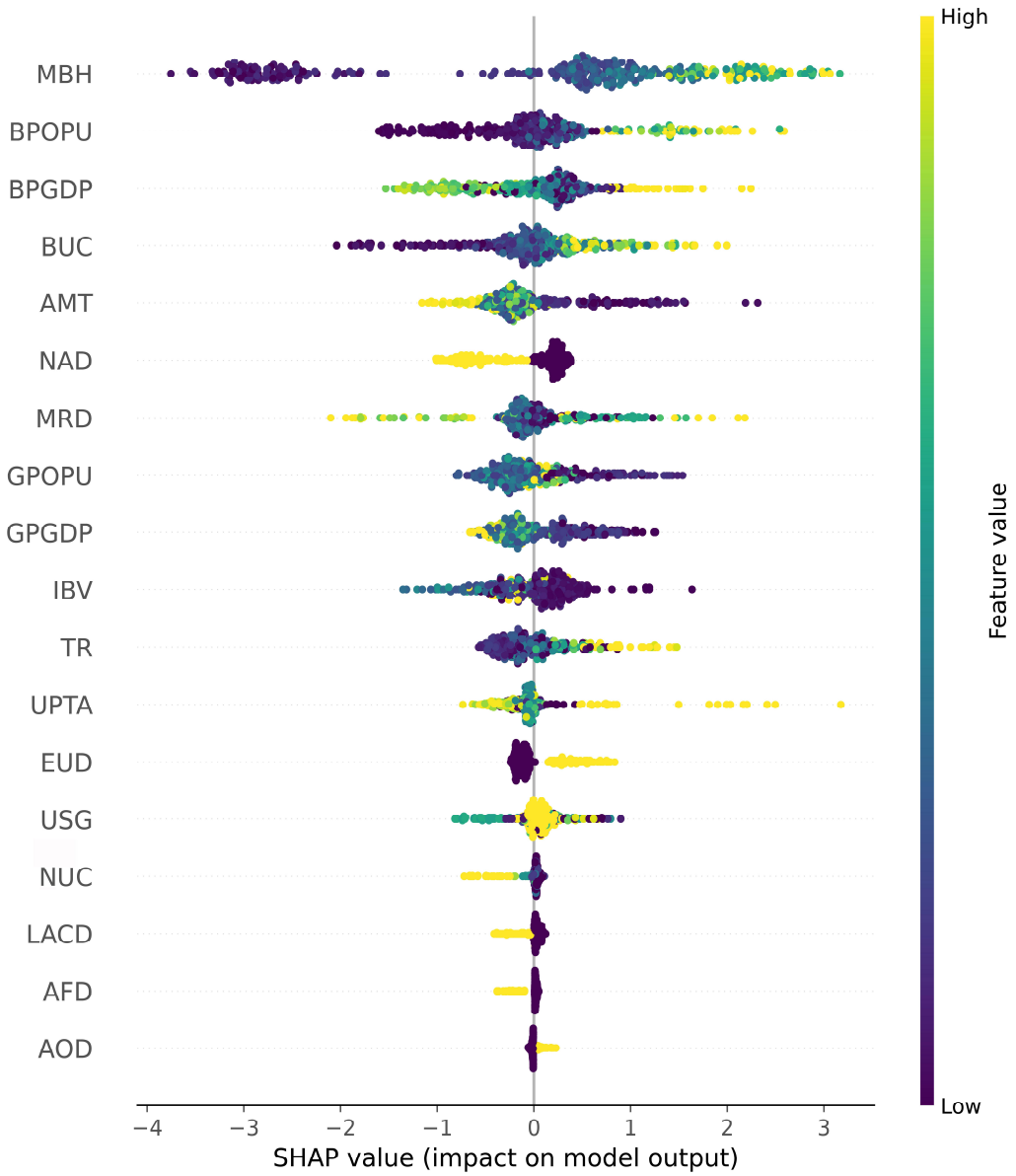
Supplementary Figure 9. Geographical distribution of 3D urban expansion patterns in Brazil and South America. Each dot represents a sample city. Maps were created using ArcGIS® software by Esri. Basemap polygon data source: Resource and Environmental Science Data Platform (https://www.resdc.cn/data.aspx?DATAID=205)



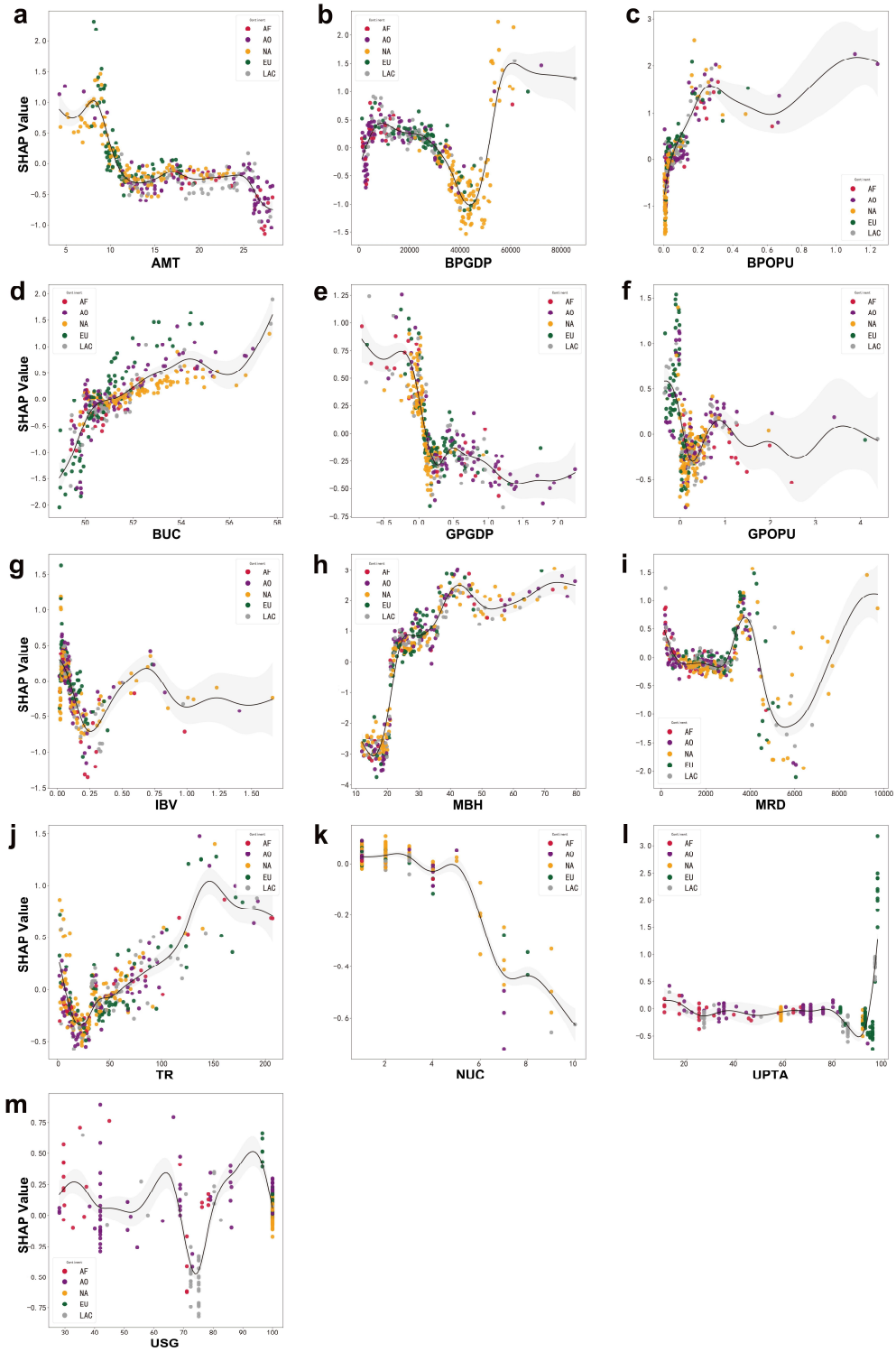
Supplementary Figure 10. Geographical distribution of 3D urban expansion patterns in West Africa. Each dot represents a sample city. Maps were created using ArcGIS® software by Esri. Basemap polygon data source: Resource and Environmental Science Data Platform (https://www.resdc.cn/data.aspx?DATAID=205)



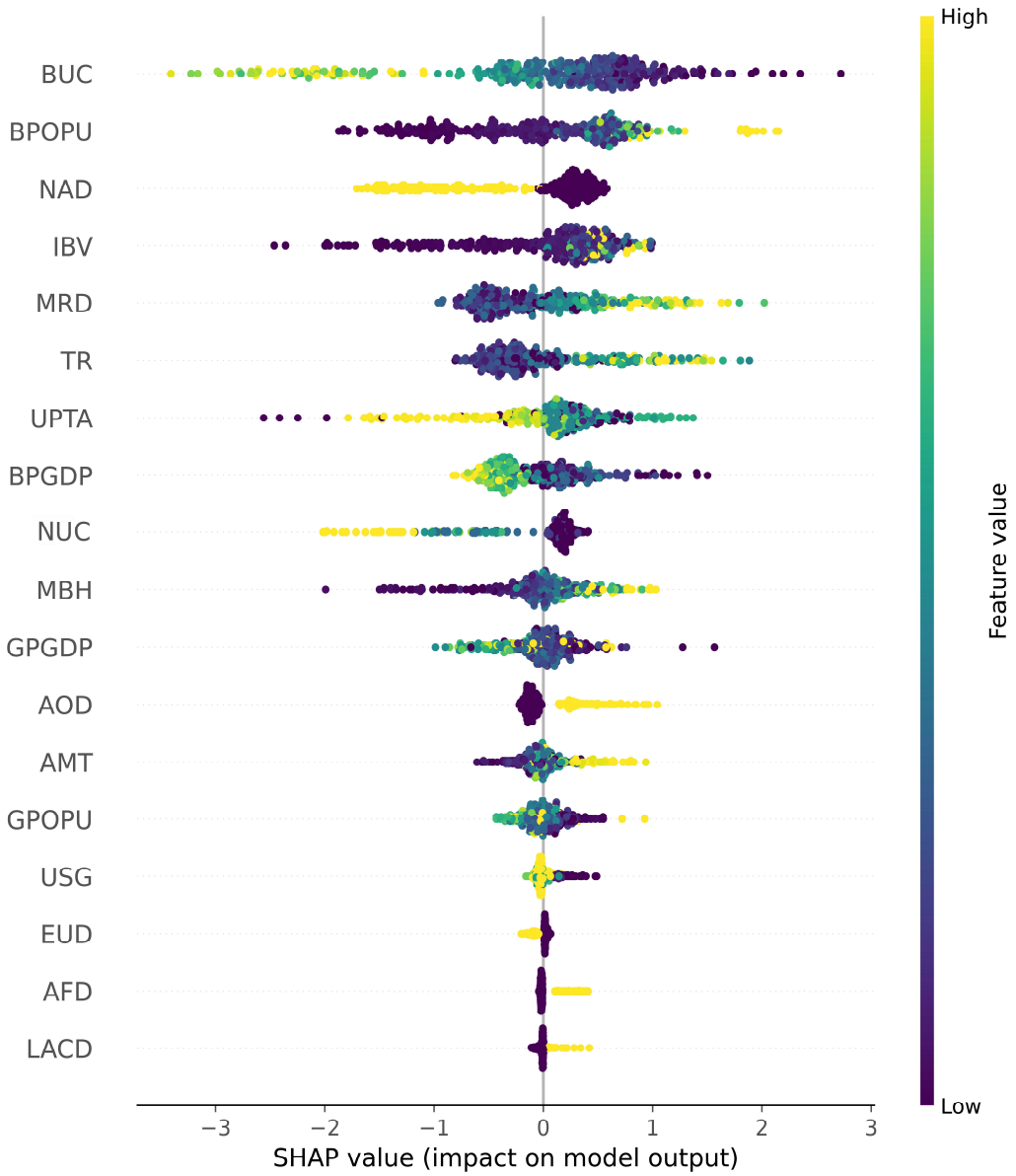
Supplementary Figure 11. Geographical distribution of 3D urban expansion patterns in Western Europe. Each dot represents a sample city. Maps were created using ArcGIS® software by Esri. Basemap polygon data source: Resource and Environmental Science Data Platform (https://www.resdc.cn/data.aspx?DATAID=205)



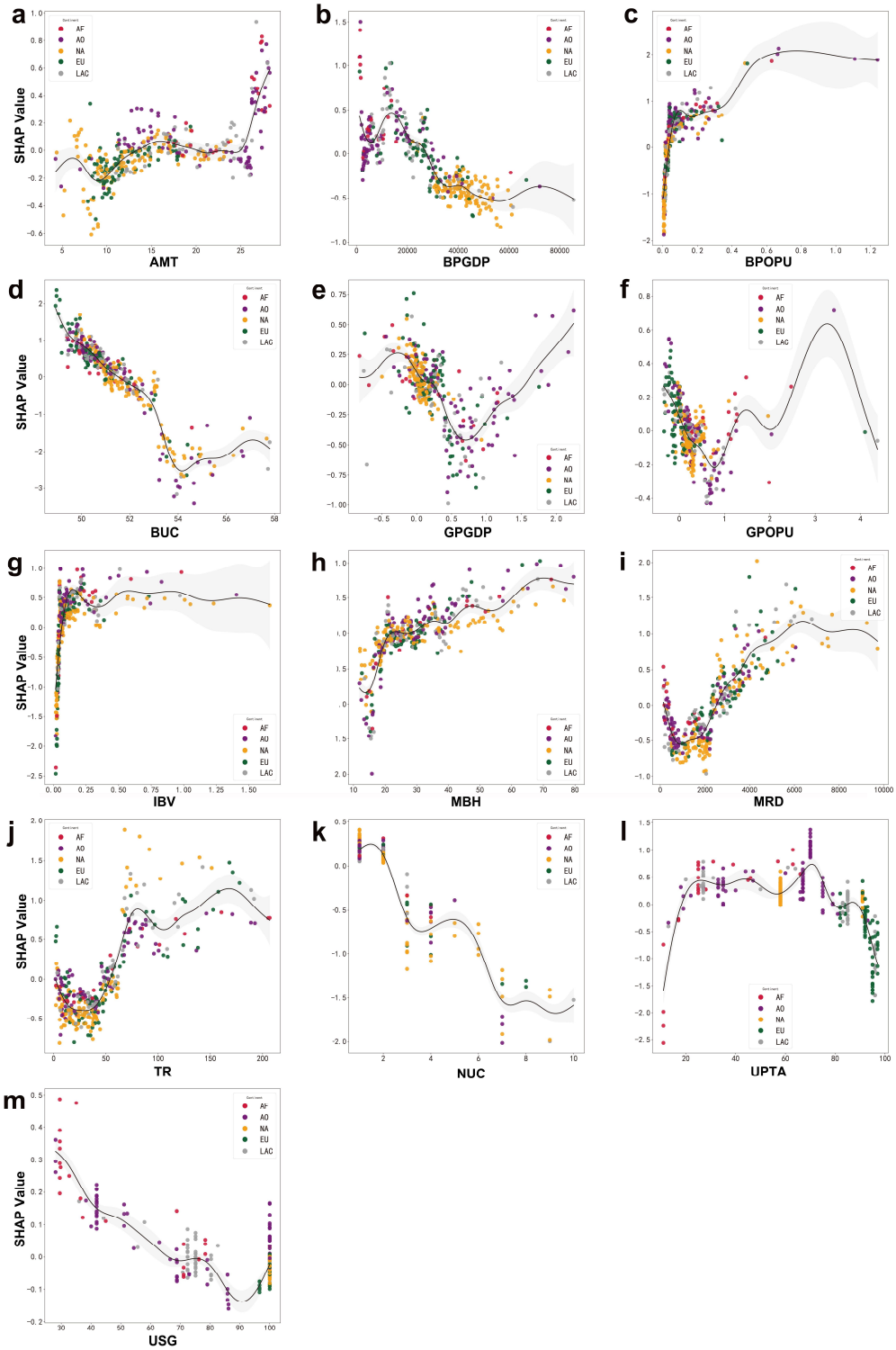
Supplementary Figure 12. SHAP value distribution of all features for the HC-HI pattern. Each dot represents a specific sample, with the color indicating the feature value. A positive SHAP value indicates that the feature contributes positively to the prediction (i.e., increases the probability of the sample being classified into the pattern), while a negative SHAP value reflects a negative contribution (i.e., decreases the probability of the pattern prediction).



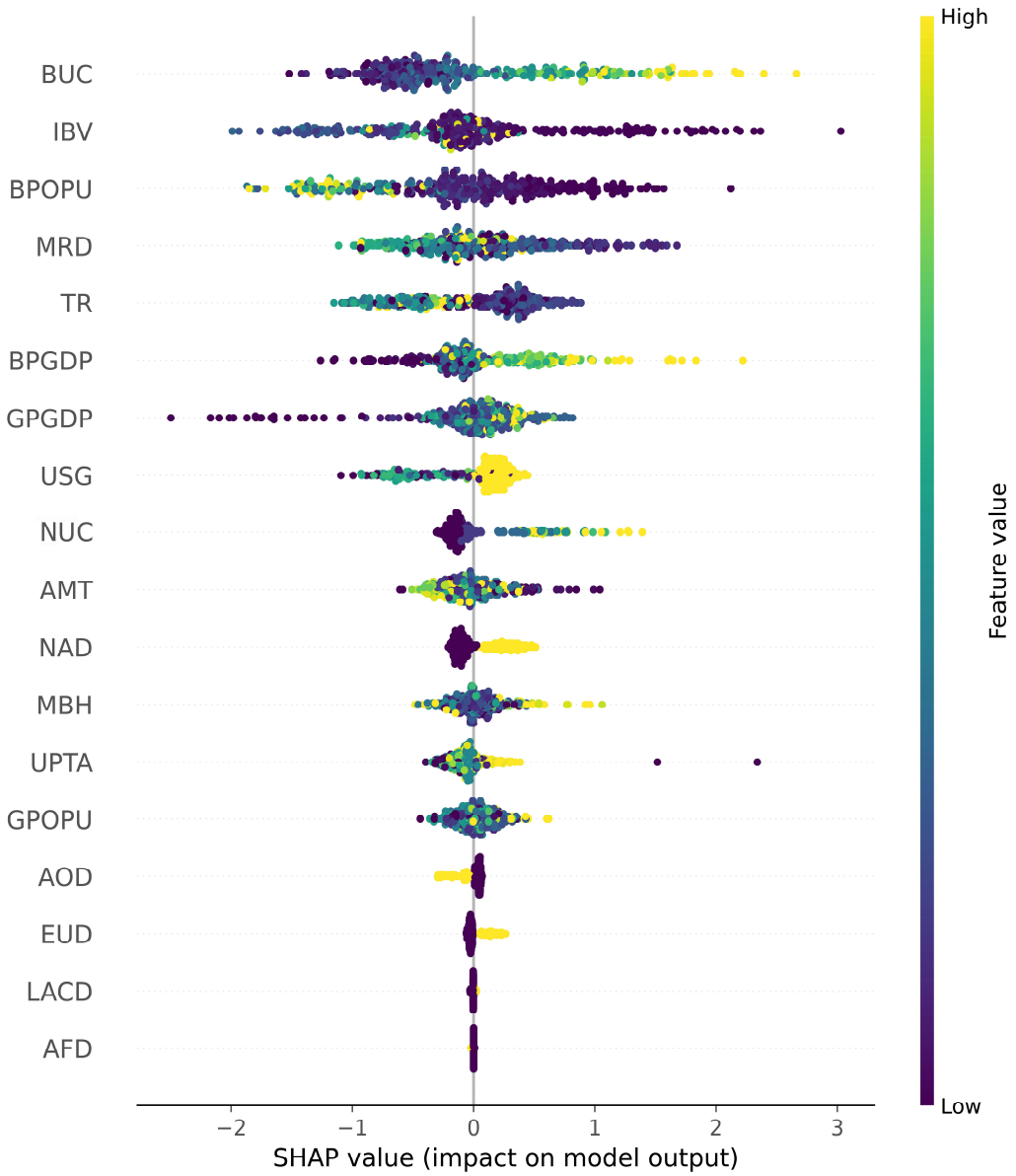
Supplementary Figure 13. The relationship between feature values and SHAP values for the HC-HI pattern. a for Annual Mean Temperature. **b** for Baseline Per Capita GDP. **c** for Baseline Population. **d** for Baseline Urban Centrality. **e** for Growth Rate of Per Capita GDP. **f** for Growth Rate of Population. **g** for Increased Built-up Volume. **h** for Maximum Building Height. **i** for Motor Roadway Density. **j** for Terrain Relief. **k** for Number of Urban Centers. **l** for Urban Public Transit Accessibility. **m** for Urban Slum Governance. The curve shows Generalized Additive Model fitting.



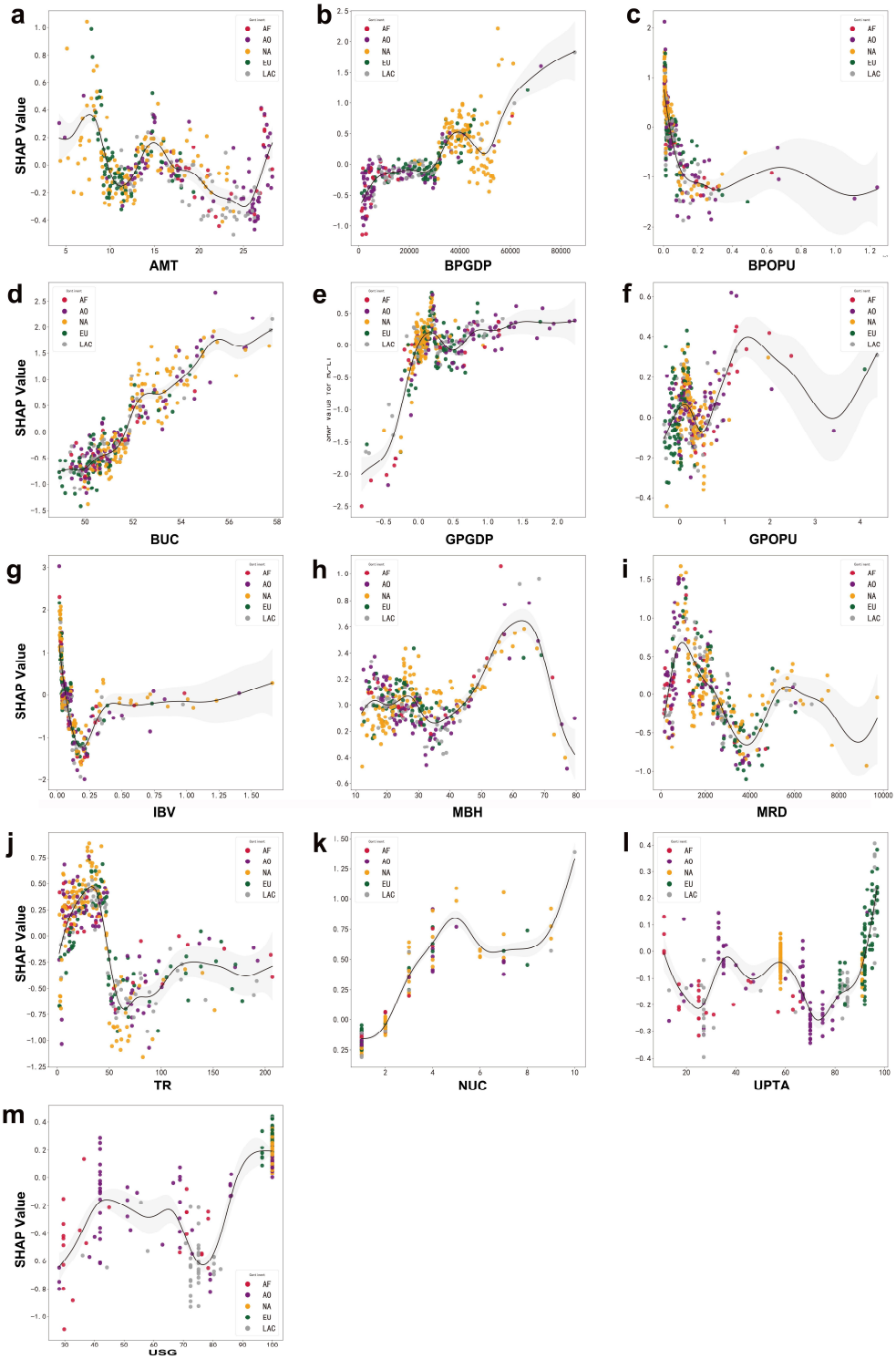
Supplementary Figure 14. SHAP value distribution of all features for the LC-HI pattern. Each dot represents a specific sample, with the color indicating the feature value. A positive SHAP value indicates that the feature contributes positively to the prediction (i.e., increases the probability of the sample being classified into the pattern), while a negative SHAP value reflects a negative contribution (i.e., decreases the probability of the pattern prediction).



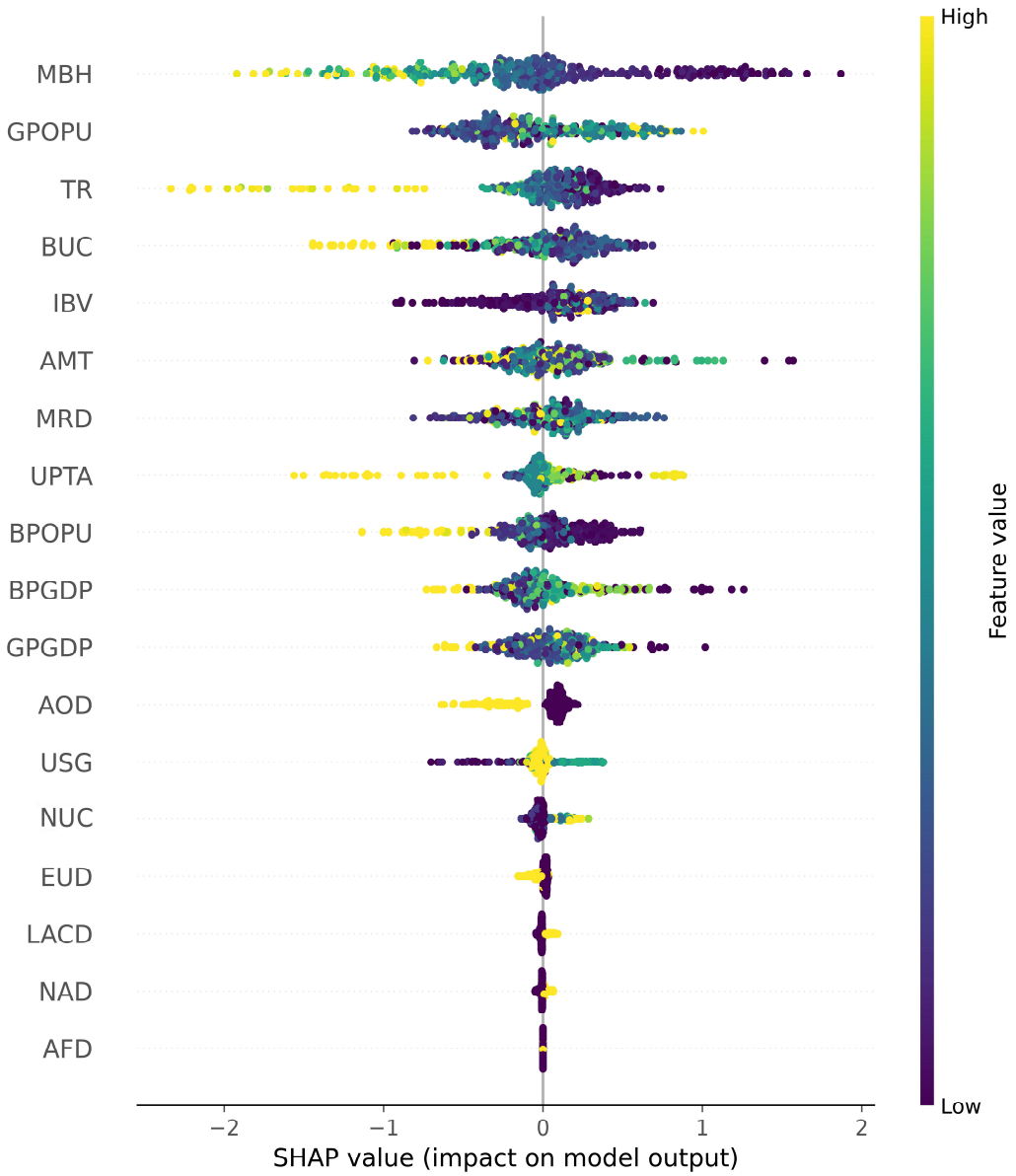
Supplementary Figure 15. The relationship between feature values and SHAP values for the LC-HI pattern. a for Annual Mean Temperature. **b** for Baseline Per Capita GDP. **c** for Baseline Population. **d** for Baseline Urban Centrality. **e** for Growth Rate of Per Capita GDP. **f** for Growth Rate of Population. **g** for Increased Built-up Volume. **h** for Maximum Building Height. **i** for Motor Roadway Density. **j** for Terrain Relief. **k** for Number of Urban Centers. **l** for Urban Public Transit Accessibility. **m** for Urban Slum Governance. The curve shows Generalized Additive Model fitting.



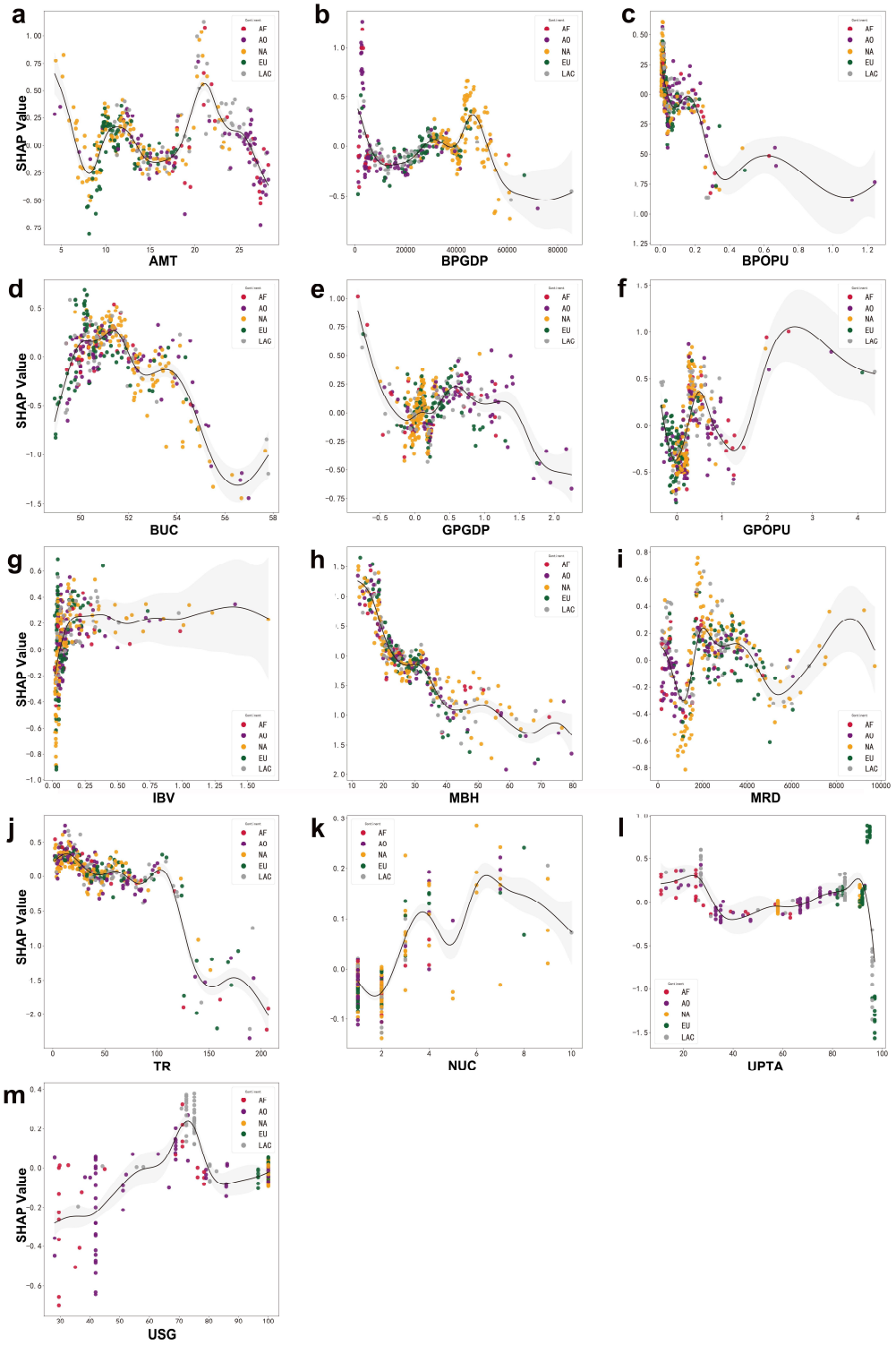
Supplementary Figure 16. SHAP value distribution of all features for the HC-LI pattern. Each dot represents a specific sample, with the color indicating the feature value. A positive SHAP value indicates that the feature contributes positively to the prediction (i.e., increases the probability of the sample being classified into the pattern), while a negative SHAP value reflects a negative contribution (i.e., decreases the probability of the pattern prediction).



Supplementary Figure 17. The relationship between feature values and SHAP values for the HC-LI pattern. a for Annual Mean Temperature. **b** for Baseline Per Capita GDP. **c** for Baseline Population. **d** for Baseline Urban Centrality. **e** for Growth Rate of Per Capita GDP. **f** for Growth Rate of Population. **g** for Increased Built-up Volume. **h** for Maximum Building Height. **i** for Motor Roadway Density. **j** for Terrain Relief. **k** for Number of Urban Centers. **l** for Urban Public Transit Accessibility. **m** for Urban Slum Governance. The curve shows Generalized Additive Model fitting.



Supplementary Figure 18. SHAP value distribution of all features for the LC-LI pattern. Each dot represents a specific sample, with the color indicating the feature value. A positive SHAP value indicates that the feature contributes positively to the prediction (i.e., increases the probability of the sample being classified into the pattern), while a negative SHAP value reflects a negative contribution (i.e., decreases the probability of the pattern prediction).



Supplementary Figure 19. The relationship between feature values and SHAP values for the LC-LI pattern. a for Annual Mean Temperature. **b** for Baseline Per Capita GDP. **c** for Baseline Population. **d** for Baseline Urban Centrality. **e** for Growth Rate of Per Capita GDP. **f** for Growth Rate of Population. **g** for Increased Built-up Volume. **h** for Maximum Building Height. **i** for Motor Roadway Density. **j** for Terrain Relief. **k** for Number of Urban Centers. **l** for Urban Public Transit Accessibility. **m** for Urban Slum Governance. The curve shows Generalized Additive Model fitting.

Supplementary Table 1. Top 50 cities with the highest 3D-based CI scores.

City	Country	3D-based CI Rank	2D-based CI Rank	3D-based CI	2D-based CI
Ekibastuz	Kazakhstan	1	1	81.921	76.317
Jungar	China	2	3	74.822	69.059
Mezhdurechensk	Russia	3	2	74.186	69.558
Dahej	India	4	5	69.465	64.249
Amarah	Iraq	5	4	68.583	65.267
Zhaozhou	China	6	10	66.718	58.678
Riobamba	Ecuador	7	6	63.939	60.119
Jiuquan	China	8	8	63.917	59.495
Shanwei	China	9	86	63.207	53.476
Grand Forks	United States	10	9	63.113	59.280
Nong'an	China	11	25	62.666	55.799
Sargodha	Pakistan	12	11	62.657	58.070
Manhattan	United States	13	20	62.104	56.346
Jhajjar	India	14	13	62.056	57.845
Sucre	Bolivia	15	22	61.876	56.128
Suez	Egypt	16	15	61.802	57.691
Changfeng	China	17	36	61.706	55.151
Huailai	China	18	50	61.660	54.354
Ningjiang	China	19	24	61.506	55.975
Kut	Iraq	20	17	61.338	57.466
Hotan	China	21	38	61.265	55.044
Lushan	China	22	19	61.177	56.415
Jiyang	China	23	39	61.089	55.018
Zhaoyuan	China	24	61	60.915	53.981
Dunhua	China	25	34	60.880	55.240
Columbia(South Carolina)	United States	26	43	60.867	54.769
Queshan	China	27	31	60.609	55.428
Petrolina	Brazil	28	12	60.439	57.857
Minggang	China	29	113	60.329	52.914
Gwalior	India	30	21	60.285	56.223
Basra	Iraq	31	32	60.171	55.375
Otradnoe	Russia	32	42	60.033	54.809
Palermo	Italy	33	303	60.023	51.109
Lumberton	United States	34	59	60.008	54.088
Dhanbad	India	35	70	59.939	53.798

City	Country	3D-based CI Rank	2D-based CI Rank	3D-based CI	2D-based CI
Karamay	China	36	30	59.926	55.499
Aqaba	Jordan	37	7	59.843	60.038
Almalyk	Uzbekistan	38	16	59.701	57.683
Al Mafraq	Jordan	39	33	59.672	55.345
Iquique	Chile	40	14	59.657	57.713
Trapani	Italy	41	109	59.563	52.968
Porlamar	Venezuela	42	53	59.437	54.281
Zhaodong	China	43	193	59.426	51.818
Guang'an	China	44	45	59.422	54.712
Huanggang	China	45	255	59.229	51.363
Laoling	China	46	87	59.173	53.463
Mengzi	China	47	78	59.101	53.681
Lingbi	China	48	127	59.086	52.755
Wilson	United States	49	65	59.069	53.852
Qingxian	China	50	77	59.045	53.728

Supplementary Table 2. Population distribution of sample cities by continent.

Continent	Population size in 2018	Number of sample cities	Ratio (%)
North America	5m+	9	2.37
	1m-5m	37	9.74
	0.5-1m	37	9.74
	0.1-0.5m	164	43.16
	0.1m-	133	35.00
Latin America and the Caribbean	5m+	7	4.05
	1m-5m	47	27.17
	0.5-1m	44	25.43
	0.1-0.5m	74	42.77
	0.1m-	1	0.58
Europe	5m+	4	1.07
	1m-5m	48	12.87
	0.5-1m	62	16.62
	0.1-0.5m	233	62.47
	0.1m-	26	6.97
Asia & Oceania	5m+	41	5.23
	1m-5m	163	20.79
	0.5-1m	152	19.39
	0.1-0.5m	384	48.98
	0.1m-	44	5.61
Africa	5m+	5	4.55
	1m-5m	41	37.27
	0.5-1m	26	23.64
	0.1-0.5m	34	30.91
	0.1m-	4	3.64

Supplementary Table 3. Cities with no intersection of population and light center.

City	Continent	Country
Ibadan	Africa	Nigeria
Rotterdam	Europe	Netherlands
Chattogram	Asia & Oceania	Bangladesh
Rabat	Africa	Morocco
Xiamen	Asia & Oceania	China
Mogadishu	Africa	Somalia
Tongi	Asia & Oceania	Bangladesh
San Salvador	Latin America and the Caribbean	El Salvador
Onitsha	Africa	Nigeria
Cheongju	Asia & Oceania	South Korea
Ulsan	Asia & Oceania	South Korea
Blantyre	Africa	Malawi
Vanderbijlpark	Africa	South Africa
Bonn	Europe	Germany
Tampico	Latin America and the Caribbean	México
Enugu	Africa	Nigeria
Jeonju	Asia & Oceania	South Korea
Warri	Africa	Nigeria
Samarinda	Asia & Oceania	Indonesia
Xianyou	Asia & Oceania	China
Duqiao	Asia & Oceania	China
Sana’a	Asia & Oceania	Yemen
Cheonan	Asia & Oceania	South Korea
Konya	Asia & Oceania	Turkey
Sanya	Asia & Oceania	China
Yiyang	Asia & Oceania	China
Qitaihe	Asia & Oceania	China
La Serena-Coquimbo	Latin America and the Caribbean	Chile
Concepcion	Latin America and the Caribbean	Chile
Suk Chai	Asia & Oceania	Thailand
Windhoek	Africa	Namibia
Fuzhou	Asia & Oceania	China
Kemerovo	Europe	Russia
Durgapur	Asia & Oceania	India
Franco da Rocha	Latin America and the Caribbean	Brazil
Asahikawa	Asia & Oceania	Japan
Yizheng	Asia & Oceania	China
Palma	Europe	Spain
Limeira	Latin America and the Caribbean	Brazil
Punto Fijo	Latin America and the Caribbean	Venezuela
eMalahleni	Africa	South Africa

City	Continent	Country
Luton	Europe	United Kingdom
Kolwezi	Africa	Democratic Republic of the Congo
Zhoushan	Asia & Oceania	China
Skikda	Africa	Algeria
EI Tigre	Latin America and the Caribbean	Venezuela
Anqiu	Asia & Oceania	China
Jingmen	Asia & Oceania	China
Kurashiki	Asia & Oceania	Japan
Doumen	Asia & Oceania	China
Jiayuguan	Asia & Oceania	China
Fukuyama	Asia & Oceania	Japan
Paramaribo	Latin America and the Caribbean	Suriname
Cuautla	Latin America and the Caribbean	México
Babruysk	Europe	Belarus
Zaozhuang	Asia & Oceania	China
Middelburg	Africa	South Africa
Manly	Asia & Oceania	Australia
Ssbokeng	Africa	South Africa
Yan'An	Asia & Oceania	China
Heerlen	Europe	Netherlands
Nanyu	Asia & Oceania	China
Wendeng	Asia & Oceania	China
Chiautempan	Latin America and the Caribbean	México
Pakuro	Africa	Nigeria
Angarsk	Europe	Russia
Le Havre	Europe	France
Neyveli	Asia & Oceania	India
Glenfield	Asia & Oceania	New Zealand
Alkmaar	Europe	Netherlands
Navoi	Asia & Oceania	Uzbekistan
Kulim	Asia & Oceania	Malaysia
Kambah	Asia & Oceania	Australia
Yongchuan	Asia & Oceania	China
Sandakan	Asia & Oceania	Malaysia
Rostock	Europe	Germany
Salinas	North America	United States
Peterborough	Europe	United Kingdom
Quang Hanh	Asia & Oceania	Vietnam
Wollongong	Asia & Oceania	Australia
Dunkirk	Europe	France
Junan	Asia & Oceania	China

City	Continent	Country
Odense	Europe	Denmark
Bruges	Europe	Belgium
Khurianwala-Balochhi	Asia & Oceania	Pakistan
San Benedetto-Giulianova	Europe	Italy
Jiaocheng	Asia & Oceania	China
Mianchi	Asia & Oceania	China
Tula	Latin America and the Caribbean	México
Yongcheng	Asia & Oceania	China
Nankang	Asia & Oceania	China
Joetsu	Asia & Oceania	Japan
Minab	Asia & Oceania	Iran
Maryvilla-Moraira	Europe	Spain
Gaochun	Asia & Oceania	China
Baytown-Mont Belvieu	North America	United States
Frederick	North America	United States
Novolugovoe	Europe	Russia
Dongming	Asia & Oceania	China
Cairns	Asia & Oceania	Australia
Lingshan	Asia & Oceania	China
Vasteras	Europe	Sweden
Yandian	Asia & Oceania	China
Brantford	North America	Canada
Sunshine Coast	Asia & Oceania	Australia
Hengdian	Asia & Oceania	China
Tracy	North America	United States
Mt Pleasant	North America	United States
Sete	Europe	France
Longmont	North America	United States
Boxing	Asia & Oceania	China
Al Madina	Asia & Oceania	Iraq
Tauranga	Asia & Oceania	New Zealand
Xiangyuan	Asia & Oceania	China
Ballarat	Asia & Oceania	Australia
Guanzhuang	Asia & Oceania	China
Beaumont	North America	United States
Mandeville	North America	United States
Lima	North America	United States
Awaza-Turkmenbashi	Asia & Oceania	Turkmenistan
Kamisu	Asia & Oceania	Japan
Sangatta	Asia & Oceania	Indonesia
Gong Badak	Asia & Oceania	Malaysia
Liugezhuang	Asia & Oceania	China

Supplementary Table 4. Detailed information of variables of the LightGBM model.

Variable	Data source	Note
Terrain Relief (TR)	GTOPO30 (https://globalmaps.github.io/el.html#summary)	It is calculated by taking the average of the difference between the maximum and minimum elevations within a radius of 4*4 km around each grid within the city boundary.
Annual Mean Temperature (AMT)	CRU TS v4 (Ref.1) (https://crudata.uea.ac.uk/cru/data/hrg)	It is the average of the mean temperature in March, June, September and December for the years 2000 and 2018, based on the gridded temperature data from CRU TS v4.
Baseline Population (BPOPU)	LandScan data of 2000 (https://landscan.ornl.gov)	The population data is calculated by taking the sum of the population grid values within the city boundary.
Baseline Per Capita GDP (BPGDP)	Gridded global datasets for Gross Domestic Product of 2000 (Ref. 2) (https://doi.org/10.5061/dryad.dk1j0)	The GDP data is calculated by summing the GDP (purchasing power parity) grid values within the city boundaries.
Growth Rate of Per Capita GDP (GPGDP)	Gridded global datasets for Gross Domestic Product of 2000 and 2015; LandScan data of 2000 and 2015	We calculate GDP growth rates from 2000 to 2015 since 2018 data is missing from this dataset.
Growth Rate of Population (GPOPU)	LandScan data of 2000 and 2015	We calculate population growth rates from 2000 to 2015 in order to align it with the time period of GDP growth data.
Maximum Building Height (MBH)	GHS-BUILT-H data of 2018 (https://human-settlement.emergency.copernicus.eu/datasets.php)	It is the maximum grid height value within the urban centers of each city in 2018, derived from the GHS-BUILT-H data.
Baseline Urban Centrality (BUC)	Global Urban Boundaries data of 2000 (https://data-starcloud.pcl.ac.cn/zh/resource/14)； GHS-BUILT-S data of 2000 (https://human-settlement.emergency.copernicus.eu/datasets.php); LandScan data of 2000 (https://landscan.ornl.gov);	There may be multiple built-up areas within the sample cities in 2000; we select the one with the largest area as the subject of analysis. We then identify the urban centers and calculate the centrality index based on the GHS-BUILT-S data from 2000.
Increased Built-up Volume (IBV)	Global Urban Boundaries data of 2018; GHS-BUILT-S data of 2000 and 2018; GHS-BUILT-H data of 2018	It is derived through the process of calculating II.

Variable	Data source	Note
Number of Urban Centers (NUC)	LandScan data of 2018 (https://landscan.ornl.gov); NPP-VIIRS-like NTL data of 2017, 2018 and 2019 (https://dataverse.harvard.edu/dataset.xhtml?persistentId=doi:10.7910/DVN/YGIVCD)	It is derived through the process of calculating CI.
Motor Roadway Density (MRD)	GRIP global roads database (Ref. 3) (https://www.globio.info/download-grip-dataset)	It is calculated by taking the mean value of the road density grid within the city boundary.
Urban Public Transit Accessibility (UPTA)	Sustainable Development Report 2024(https://dashboards.sdgindex.org/explorer)	It is a country-level indicator calculated based on the proportion of the urban population living in slums.
Urban Slum Governance (USG)	Sustainable Development Report 2024(https://dashboards.sdgindex.org/explorer)	It is a country-level indicator calculated based on the population with convenient access to public transport in cities.
Asia and Oceania Dummy (AOD)	-	The value is 1 if the city is located in Asia and Oceania, and 0 if not.
Africa Dummy (AFD)	-	The value is 1 if the city is located in Africa, and 0 if not.
Europe Dummy (EUD)	-	The value is 1 if the city is located in Europe, and 0 if not.
North America Dummy (NAD)	-	The value is 1 if the city is located in North America, and 0 if not.
Latin America and the Caribbean Dummy (LACD)	-	The value is 1 if the city is located in Latin America and the Caribbean, and 0 if not.

Supplementary Note 1. Independence Tests between 2D- and 3D-based CI

To assess whether the 3D-based Centrality Index (3D-based CI) captures unique spatial information beyond that already reflected in the 2D-based Centrality Index (2D-based CI), we conducted several diagnostic analyses.

Correlation and Condition Index

The Pearson correlation coefficient between 3D-based CI and 2D-based CI is 0.916 ($p < 0.001$), confirming a strong linear relationship. However, the condition index derived from the eigenvalues of the correlation matrix equals 22.85 (< 30), which is below the common multicollinearity threshold, indicating that the two indices are correlated but not redundant.

Residual Analysis

The residual analysis was conducted by the following linear regression model:

$$CI_{3D} = \alpha + \beta\ CI_{2D} + \varepsilon \quad (1)$$

where the residuals (ε) was extracted to quantify the variation in 3D-based CI unexplained by 2D-based CI. The residuals exhibit substantial positive and negative deviations across cities, suggesting meaningful divergence from purely horizontal patterns. The variance of the residuals (1.6) relative to the original 3D-based CI variance (9.8) indicates that approximately 16% of the total variance in 3D-based CI cannot be explained by 2D-based CI. This portion can be interpreted as the independent contribution of vertical structure to overall spatial concentration.

Together, these results demonstrate that while 3D-based CI and 2D-based CI are strongly correlated—as expected given that building volume derives from footprint and height—the 3D-based CI retains statistically significant independent variation. This independent component reflects how vertical concentration modifies or amplifies horizontal spatial patterns, especially in cities where high-rise clusters emerge unevenly within the built-up area. Hence, the 3D-based CI should not be viewed as a redundant extension of 2D-based CI, but rather as a complementary measure capturing the volumetric dimension of urban centrality.

Supplementary Note 2. Independence Tests between 3D-based CI and II

Given that both the 3D-based Centrality Index (3D-based CI) and the Intensity Index (II) are derived from built-up volume data, we conducted statistical tests to determine whether they capture independent aspects of vertical urban structure.

Correlation Analysis

The Pearson correlation coefficient between 3D-based CI and II is −0.203 ($p < 0.001$), indicating a weak negative correlation. This suggests that, globally, cities with highly centralized 3D structures (high CI) do not necessarily exhibit high average vertical intensity (high II). In some cases, highly centralized cities may feature compact yet moderately tall cores, whereas dispersed urban areas may contain isolated but tall peripheral clusters.

Partial Correlation and Residual Analysis

We further conducted a residual-based diagnostic test using the regression:

$$CI_{3D} = \alpha + \beta\ II + \varepsilon \qquad (2)$$

where the residuals (ε) was extracted to quantify the variation in 3D-based CI unexplained by II. The residuals exhibit substantial positive and negative deviations across cities, suggesting meaningful divergence from purely horizontal patterns. The variance of the residuals (9.4) relative to the original 3D-based CI variance (9.8) indicates that approximately 96% of the total variance in 3D-based CI cannot be explained by II. This confirms that the two indicators are not structurally redundant, but instead represent distinct dimensions of urban volumetric structure: 3D-based CI emphasizes the spatial concentration of built-up volume, and II reflects the average vertical intensity of that volume.

The above results empirically validate that combining CI and II provides complementary insights into 3D urban expansion. Specifically, the four-pattern typology (HC-HI, HC-LI, LC-HI, LC-LI) captures both where volumetric concentration occurs and how strongly it is expressed in the vertical dimension, rather than being an artifact of shared data structure.

Supplementary Note 3. Robustness Tests of Classification Methods

To ensure the robustness of the four-category framework used to identify 3D urban growth patterns, we conducted a sensitivity analysis based on alternative classification methods. Specifically, two additional classification schemes were tested: (1) median-based categorization, and (2) hierarchical clustering-based categorization. These were compared with the baseline mean-value classification adopted in the main analysis (see Fig. 2b).

Alternative classification methods

The median-based categorization replaces the mean values of CI and II with their respective medians, dividing cities into four quadrants based on whether their CI and II values are above or below the global median. This approach provides a robustness check against potential skewness in the distribution of either indicator.

The hierarchical clustering method, in contrast, does not rely on predefined thresholds but groups cities according to the similarity of their CI-II combinations. This method was selected because it captures the internal structure of the data more flexibly and is suitable when the variables may exhibit non-linear associations.

We adopted Ward's linkage criterion, which minimizes within-cluster variance and tends to produce compact, spherical clusters. Based on the dendrogram and the average silhouette score, a four-cluster solution was identified as the most interpretable and consistent with the two-dimensional typology used in the main text. For comparability, the resulting clusters were relabeled according to the relative levels of CI and II as: HC-HI, HC-LI, LC-HI, and LC-LI (High/Low Centrality × High/Low Intensity).

Consistency assessment using Kappa statistics

To quantify the degree of agreement between different classification schemes, we computed the Cohen's Kappa coefficient (κ). The Kappa statistic measures the agreement between two categorical variables beyond what would be expected by chance. It is calculated as:

$$\kappa = \frac{p_0 - p_e}{1 - p_e} \tag{3}$$

where p_0 represents the observed proportion of agreement between two classification schemes, and p_e denotes the expected agreement by random chance. Kappa values range from –1 to 1, where values above 0.75 indicate excellent agreement, values between 0.4–0.75 indicate moderate agreement, and values below 0.4 suggest weak consistency.

The results show that the median-based classification achieves a very high consistency with the mean-based classification (κ = 0.83), confirming that the classification results are robust to the choice of central tendency measure.

The hierarchical clustering approach exhibits a somewhat lower level of agreement (κ = 0.53), which is still within the moderate-to-high range, suggesting that while clustering identifies slightly more polarized groupings, the overall structure of city types remains stable.

A comparison of the number of cities assigned to each category under the mean-based and clustering-based schemes reveals that the clustering method produces a more polarized distribution (Supplementary Table 5). In particular, the LC-HI and LC-LI groups exhibit the largest discrepancies, reflecting the clustering algorithm's tendency to emphasize intergroup heterogeneity.

Supplementary Table 5. Category sizes across three different classification methods.

Pattern	The number of cities and its proportion		
	Mean-based classification	Median-based classification	Clustering-based classification
HC-HI	314(17.3%)	405(22.3%)	387(21.3%)
HC-LI	483(26.5%)	505(27.7%)	519(28.5%)
LC-HI	476(26.2%)	505(27.7%)	200(11.0%)
LC-LI	547(30.1%)	405(22.3%)	714(39.2%)

Spatial consistency of the classification results

Despite these numerical differences, the continental distributions of each growth pattern remain highly consistent across classification methods (Supplementary Table 6). All three schemes reveal similar spatial hierarchies:

- The HC-HI pattern is most prevalent in Asia & Oceania and Europe, followed by Latin America and the Caribbean, and least common in North America and Africa.

- The HC-LI pattern is dominant in North America, followed by Asia & Oceania and Europe, and less represented in Africa and Latin America and the Caribbean.

- The LC-HI pattern occurs primarily in Asia & Oceania, Africa, and Latin America and the Caribbean, with lower prevalence in Europe and the lowest in North America.

- The LC-LI pattern is most common in Latin America and the Caribbean, Africa, and North America, followed by Europe, and least common in Asia & Oceania.

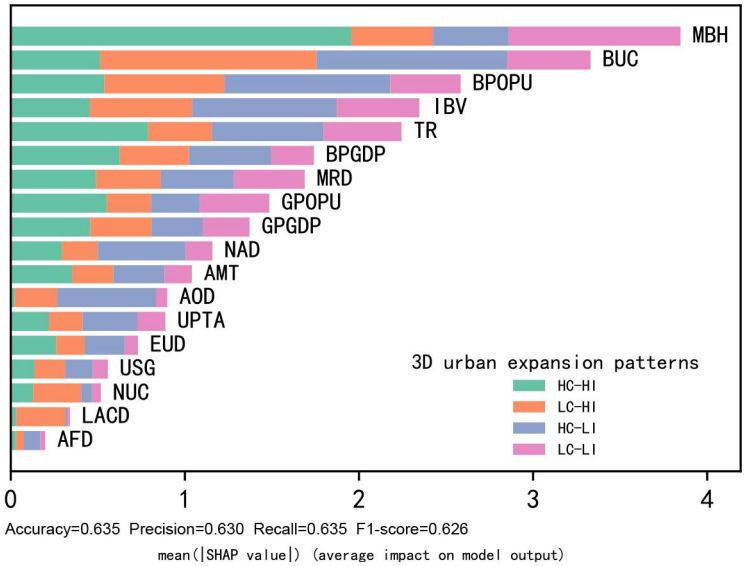
These consistent regional hierarchies reinforce the stability and interpretability of the typology under different classification criteria.

Supplementary Table 6. Regional distribution of category types under three classification methods.

Region	Classification method	Proportion of different patterns （%）			
		HC-HI	HC-LI	LC-HI	LC-LI
Africa	Mean-based	3.6	12.7	39.1	44.5
	Median-based	4.5	11.8	45.5	38.2
	Clustering-based	8.2	11.8	12.7	67.3
Latin America and the Caribbean	Mean-based	6.9	8.1	40.5	44.5
	Median-based	12.7	7.5	49.7	30.1
	Clustering-based	15.6	9.8	15.6	59.0
Asia & Oceania	Mean-based	24.5	23.0	34.3	18.2
	Median-based	30.9	21.2	35.1	12.9
	Clustering-based	27.2	30.0	16.8	26.0
North America	Mean-based	3.4	49.5	4.5	42.6
	Median-based	4.7	56.1	4.5	34.7
	Clustering-based	5.5	38.9	0.5	55.0
Europe	Mean-based	24.9	23.3	20.6	31.1
	Median-based	31.6	26.8	20.6	20.9
	Clustering-based	31.4	28.4	6.7	33.5

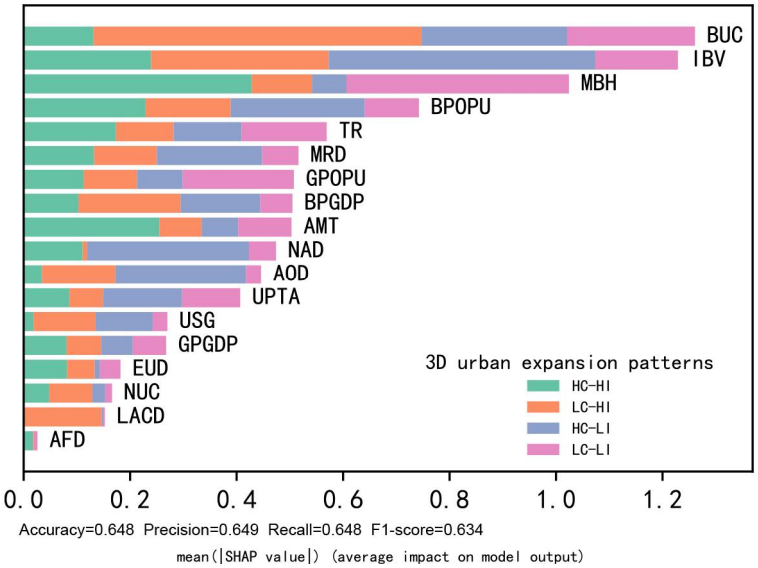
Model robustness under alternative classification methods

To further test robustness, we trained LightGBM models using the median-based and clustering-based classifications, respectively, and conducted SHAP analyses for each. In terms of variable importance, the relative ranking of predictors is highly consistent across models (see Fig. 4a, Supplementary Figures 20 and 21). In all cases, Maximum Building Height (MBH), Baseline Urban Centrality (BUC), Increased Built-up Volume (IBV), and Baseline Population (BPOPU) remain the top four predictors, demonstrating that the model's explanatory structure is robust to classification method.



Supplementary Figure 20. Ranking of the total average absolute SHAP values for

each pattern under median-based classification. For each pattern, the mean absolute SHAP value indicates the importance of each feature in predicting that pattern. Larger values signify greater importance of the feature in the model's prediction.

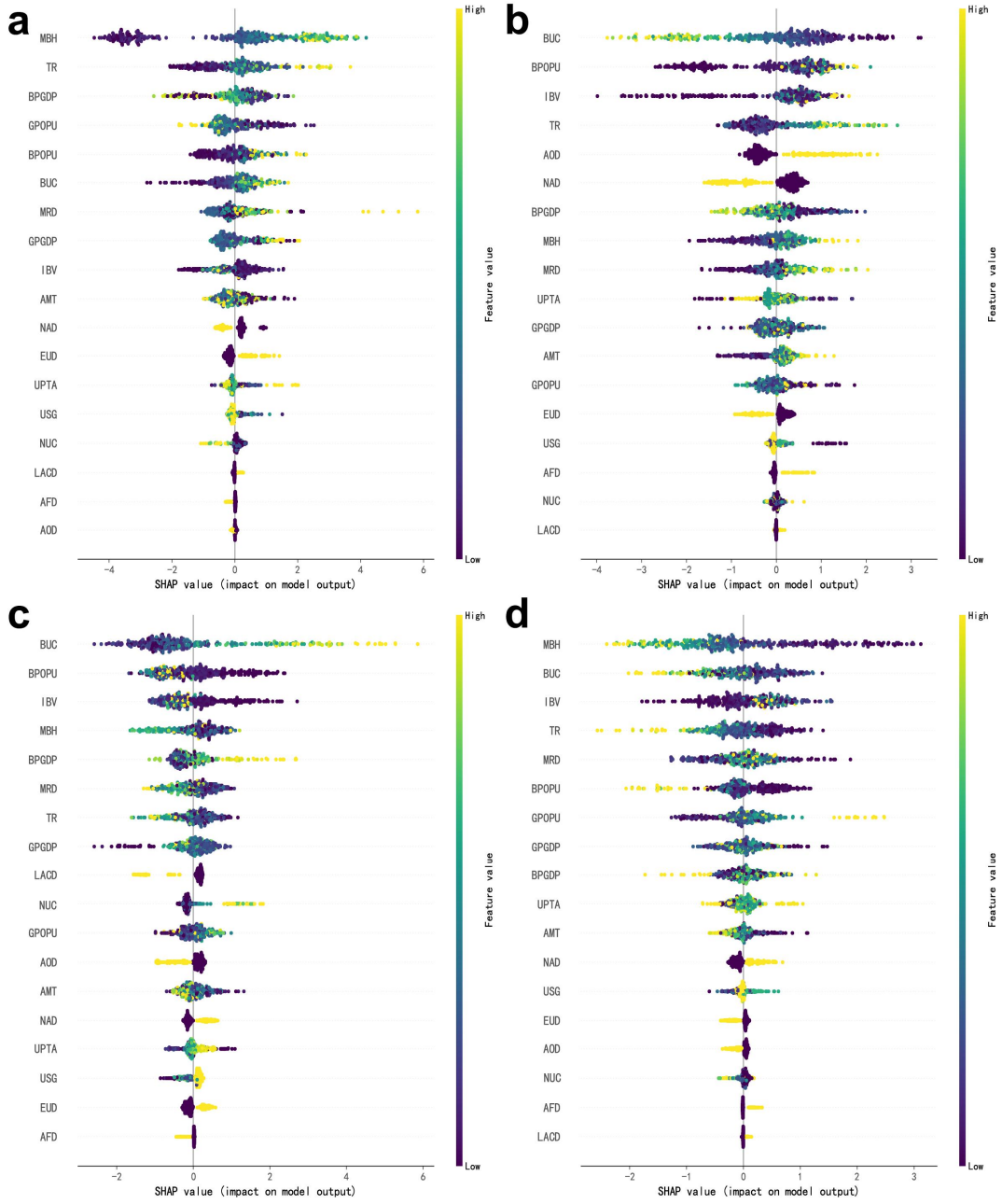


Supplementary Figure 21. Ranking of the total average absolute SHAP values for each pattern under clustering-based classification. For each pattern, the mean absolute SHAP value indicates the importance of each feature in predicting that pattern. Larger values signify greater importance of the feature in the model's prediction.

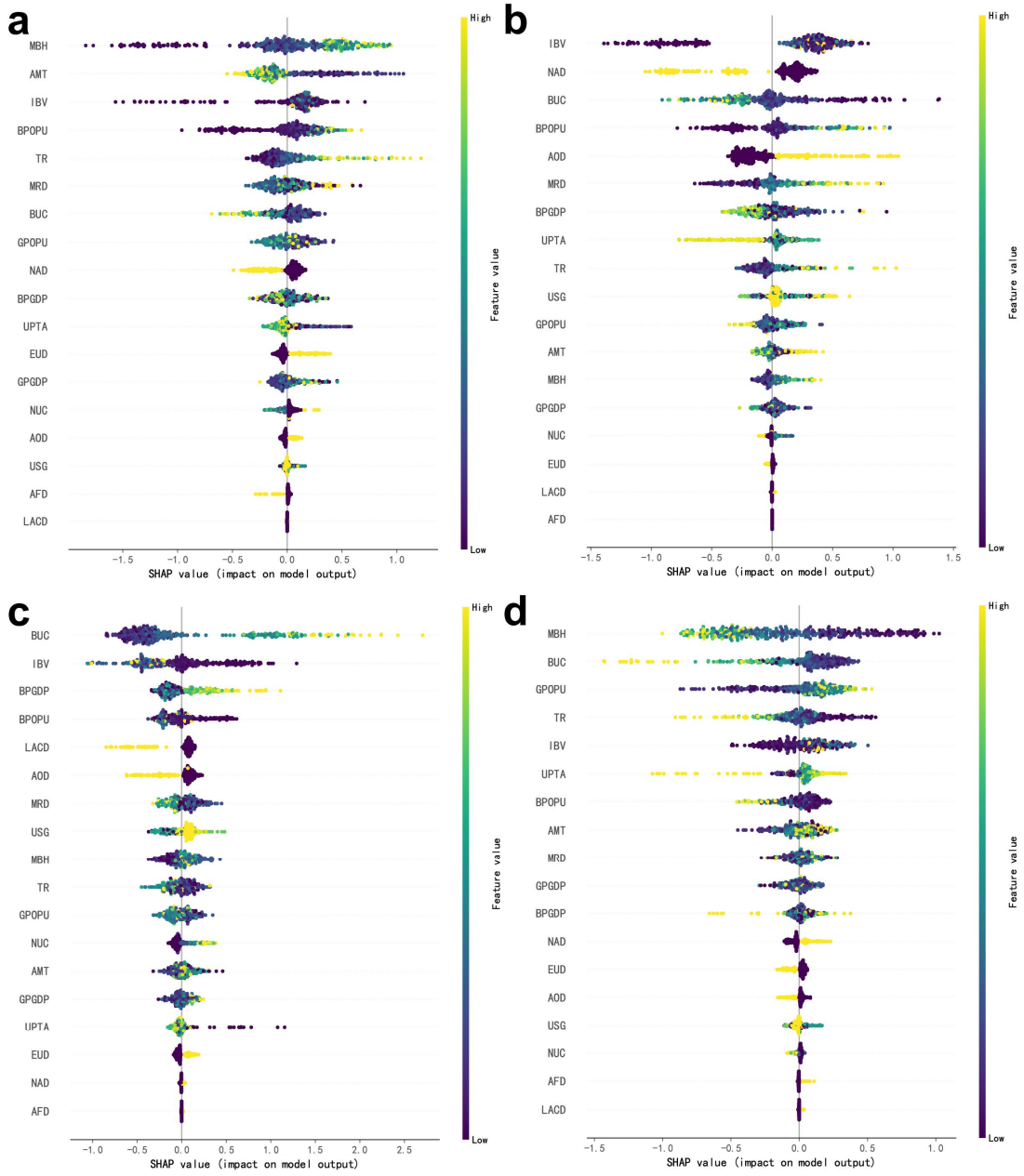
Regarding the direction of predictor effects, the relationships between variables and predicted growth patterns remain highly stable across methods (see Fig. 4b-e, Supplementary Figures 22 and 23). For example, under all classification schemes, cities exhibiting HC-HI and LC-HI patterns are associated with higher MBH values, while LC-LI cities consistently display lower MBH values.

The only notable divergence arises in the relationship between Baseline Urban Centrality (BUC) and the HC-HI pattern in the clustering-based model (Fig. S23a). In the mean- and median-based models, HC-HI cities tend to show relatively high BUC values (see Fig. 4b and Fig. S22a), whereas in the clustering-based model, they exhibit somewhat lower BUC values. This discrepancy likely results from how the clustering algorithm partitions cities near category boundaries, where compact but moderately tall cities may be reassigned to different clusters due to their mixed CI-II characteristics. Nevertheless, this exception does not alter the fundamental relationship between BUC and the overall growth typology. Across all three classification methods, HC-LI cities consistently exhibit the highest BUC levels and the strongest positive association with urban concentration, while LC-HI and LC-LI cities both show substantially lower BUC values. In other words, cities with higher baseline centrality are more likely to follow the HC-LI pattern, demonstrating a persistent positive correlation between BUC and spatial concentration of vertical growth as well as an inherent path dependency in urban development. Thus, even under the clustering-based scheme, the observed variation primarily reflects the effect of boundary reallocation rather than a reversal of underlying

relationships.



Supplementary Figure 22. SHAP value distributions for features correlating the different patterns under median-based classification. a for HC-HI. **b** for LC-HI. **c** for HC-LI. **d** for LC-LI.



Supplementary Figure 23. SHAP value distributions for features correlating the different patterns under clustering-based classification. a for HC-HI. **b** for LC-HI. **c** for HC-LI. **d** for LC-LI.

Supplementary Note 4. LightGBM Model Evaluation and Interpretation

This appendix provides a detailed account of the LightGBM multi-class model evaluation process and offers a more rigorous interpretation of the model results.

The model aims to identify potential correlates of four urban expansion patterns (HC-HI, HC-LI, LC-HI, LC-LI). To ensure the robustness of the model's performance and to prevent overfitting, we employed 10-fold cross-validation primarily for hyperparameter tuning and to assess the model's generalization capability during development. After finalizing the model's structure and hyperparameters through cross-validation, the reported overall classification accuracy of 65.1% was obtained on a held-out test set. This test set comprises data entirely unseen by the model during its training and tuning phases, thereby providing an unbiased estimate of the model's performance on new, unobserved data. Following exploratory analysis which indicated its benefit for predictive performance, we opted to exclude samples with missing values to train the final model at a higher accuracy.

The model's overall classification accuracy of 65.1%, which is substantially higher than the 25% baseline for random guessing, indicates that the selected features possess meaningful predictive power for urban expansion patterns. However, this level of accuracy also suggests that roughly one in three cities is still misclassified. Therefore, we characterize the model's performance as moderately successful, meaning that it effectively captures key associations between urban expansion patterns and the explanatory variables, but it remains imperfect. Future research could improve predictive capability by incorporating richer data dimensions, including more detailed socio-economic indicators, policy-related variables, and spatio-temporal interaction effects.

To provide a more granular view of the model's performance, we report the Precision, Recall, and F1-score for each class (Supplementary Table 7). These metrics illuminate how well the model identifies different expansion patterns, particularly for categories with smaller sample sizes. As shown in Table S7, the HC-HI pattern exhibits relatively lower predictive performance, with both precision and recall being lower than other categories, and an F1-score of 0.459. This might be attributed to the smaller sample size of this class in the dataset or significant feature overlap with other classes. This implies a higher likelihood of either false positives or false negatives when identifying this specific pattern. By contrast, the LC-LI pattern demonstrates the highest recall (0.787) and a relatively high F1-score (0.699), indicating that the model performs well in identifying true low centrality and low intensity cities, with fewer instances of false negatives. The HC-LI and LC-HI patterns show moderate performance, striking a good balance between precision and recall.

At the aggregate level, the model achieves a Macro-Averaged Precision of 0.637, Recall of 0.598, and F1-score of 0.611, reflecting its balanced capability across classes without

weighting by class size. The Weighted-Averaged Precision of 0.653, Recall of 0.651, and F1-score of 0.646 further confirm that overall performance remains stable even after accounting for class imbalance. Together, these metrics indicate that while performance varies across categories, the model maintains a consistent and reliable predictive structure overall.

Supplementary Table 7. Classification metrics for LightGBM predictions of 3D urban expansion patterns

Class	Precision	Recall	F1-score
HC-HI	0.538	0.4	0.459
HC-LI	0.698	0.638	0.667
LC-HI	0.683	0.566	0.619
LC-LI	0.629	0.787	0.699
Macro-Averaged	0.637	0.598	0.611
Weighted-Averaged	0.653	0.651	0.646

Finally, we reiterate that the LightGBM model in this study reveals associations between urban expansion patterns and a set of socio-economic and natural geographic features, rather than causal relationships. The model identifies correlational factors where different expansion patterns occur, serving as indicators for understanding their spatial distribution. However, these findings should not be directly over-interpreted as causal mechanisms without further evidence. Establishing causal links requires a more robust theoretical framework, longitudinal data analysis, and experimental or quasi-experimental designs. The insights garnered from this study provide crucial leads and a foundational basis for future research aimed at causal inference.

Supplementary Note 5. Impact Assessment of Exclusion of Urban Renewal

As noted in the main text, our study focuses exclusively on outward urban expansion—that is, the conversion of non-urban land into built-up areas—and does not capture urban renewal or densification processes occurring within existing built-up footprints. To help readers understand the quantitative scale and implications of this limitation, we provide a brief conceptual clarification and a rough estimation of the global prevalence of urban renewal during the study period (2000–2018).

Conceptual clarification

In this study, the term "urban renewal" specifically refers to the redevelopment or reconstruction of existing buildings, rather than routine renovation. Most renovation activities, such as interior upgrades, structural reinforcement, or façade improvements, do not alter the city's physical form and therefore have little impact on the spatial centrality or volumetric intensity metrics examined here.

Urban renewal, as defined in this study, is conceptually related to infill development and densification, but the concepts are not identical. Infill development—the construction of new homes within previously developed areas—includes both redevelopment of existing buildings (true urban renewal) and construction on vacant parcels within the urbanized boundary. The latter process is detectable in our data because it expands the built-up footprint. Consequently, this study primarily omits redevelopment activities that do not change the footprint, focusing instead on changes that are measurable in our spatial metrics.

Estimating the approximate share of urban renewal

Due to limited data availability, quantitative estimates of renewal's contribution to total urban growth exist primarily for the United States and China.

United States: A study conducted by the U.S. Environmental Protection Agency (EPA) found that approximately 21% of new housing construction between 2000 and 2009 occurred as infill development within already built-up areas across 209 metropolitan regions in the United States[4]. Since infill includes both redevelopment and new construction on vacant lots, the share attributable to true urban renewal is likely lower—probably below 20% of total new construction during that decade.

China: In 2023, China initiated the reconstruction of 1.59 million housing units in rundown urban areas[5]. Given the national average residential floor area of 111.18 m^2 per unit[6], this corresponds to roughly 176.8 million m^2 of rebuilt housing. By comparison, China's total new residential floor area in 2022 was approximately 1.21 billion m^2[7], implying that reconstruction accounted for around 15% of new housing activity. Since large-scale renewal in China began around 2009 with the national "shantytown redevelopment" initiative[8], the average renewal share during 2000–2018 was likely lower than this figure.

Although we lack equivalent datasets for other regions, urban renewal is generally more prevalent in developed economies due to higher land values and the ability to absorb demolition and reconstruction costs[9]. Conversely, in developing regions where land remains relatively abundant and construction costs are lower, renewal typically represents a smaller fraction of total growth.

Supporting this inference, recent global studies using multi-temporal microwave backscatter and building footprint data have mapped the relative dominance of upward (vertical) versus outward (horizontal) urban growth modes[10]. As shown in Supplementary Table 8, the ratio of upward- to outward-dominant grids is highest in advanced economies, especially in Europe and East Asia, and lowest in Latin America, India, and Africa. While "upward growth" is not synonymous with renewal—it also includes high-rise construction on newly developed land—it broadly reflects a greater prevalence of redevelopment-oriented processes in the Global North.

Overall, these sources suggest that urban renewal likely accounted for less than ~15% of total urban construction globally during the study period, with slightly higher shares in Europe and East Asia, and lower shares in Latin America, South Asia, and Africa.

Supplementary Table 8. The distribution of the ratio of upward-oriented and outward-oriented urban expansion patterns in different regions[10]

Region	The ratio of upward dominant grids to outward dominant grids during 1999-2021
Global	0.88
Advanced economies	1.02
Other economies	0.84
Africa	0.28
Australia–New Zealand	0.59
China	1.11
Europe	1.37
India	0.25
North America	0.16
Latin America	0.17
Southeast Asia	0.56

Implications for interpretation

Urban renewal primarily occurs in city centers, where older building stock and high redevelopment value coincide[9,11]. Consequently, if renewal were fully captured, we would expect the 3D-based centrality of Global North cities to be even higher, further

widening the contrasts with Global South cities observed in this study. Therefore, the exclusion of renewal implies that our analysis provides a conservative estimate of global 3D urban inequality in terms of concentration degree. Including vertical redevelopment would likely strengthen—not weaken—the study's main findings regarding more divergent patterns of urban expansion across world regions.

Supplementary References

1. Harris, I., Osborn, T. J., Jones, P. & Lister, D. Version 4 of the CRU TS monthly high-resolution gridded multivariate climate dataset. *Sci. Data* **7**, 109 (2020).
2. Kummu, M., Taka, M. & Guillaume, J. H. Gridded global datasets for gross domestic product and Human Development Index over 1990–2015. *Sci. Data* **5**, 1-15 (2018).
3. Meijer, J. R., Huijbregts, M. A. J., Schotten, K. C. G. J. & Schipper, A. M. Global patterns of current and future road infrastructure. *Environ. Res. Lett.* **13** (2018).
4. Ramsey, K. Residential Construction Trends in America's Metropolitan Regions: 2012 Edition. (U.S. Environmental Protection Agency, 2012).
5. Statistical Communiqué of the People's Republic of China on the 2023 National Economic and Social Development. (National Bureau of Statistics of China, Beijing, 2023).
6. China Population Census Yearbook 2020. (National Bureau of Statistics of China, Beijing, 2020).
7. National Real Estate Development and Sales in 2022. (National Bureau of Statistics of China, Beijing, 2022).
8. He, S. & Wu, F. China's emerging neoliberal urbanism: Perspectives from urban redevelopment. *Antipode* **41**, 282-304 (2009).
9. der Krabben, E. V. & Needham, B. Land readjustment for value capturing: a new planning tool for urban redevelopment. *Town Plan. Rev.* **79**, 651-672 (2008).
10. Frolking, S., Mahtta, R., Milliman, T., Esch, T. & Seto, K. C. Global urban structural growth shows a profound shift from spreading out to building up. *Nat. Cities* **1**, 555-566 (2024).
11. Broitman, D. & Koomen, E. The attraction of urban cores: Densification in Dutch city centres. *Urban Stud.* **57**, 1920-1939 (2020).